Atmos. Meas. Tech., 17, 3783–3807, 2024
https://doi.org/10.5194/amt-17-3783-2024

Atmospheric Measurement Techniques
Open Access
EGU

Evaluation of the hyperspectral radiometer (HSR1) at the Atmospheric Radiation Measurement (ARM) Southern Great Plains (SGP) site

Kelly A. Balmes[1,2], Laura D. Riihimaki[1,2], John Wood[3], Connor Flynn[4], Adam Theisen[5], Michael Ritsche[5], Lynn Ma[6], Gary B. Hodges[1,2], and Christian Herrera[1,2]

[1]Cooperative Institute for Research in Environmental Sciences, University of Colorado Boulder, Boulder, CO, USA
[2]Global Monitoring Laboratory, National Oceanic and Atmospheric Administration (NOAA), Boulder, CO, USA
[3]Peak Design Ltd, Sunnybank House, Wensley Rd, Winster, Derbyshire, DE4 2DH, UK
[4]School of Meteorology, University of Oklahoma, Norman, OK, USA
[5]Argonne National Laboratory, Lemont, IL, USA
[6]Brookhaven National Laboratory, Upton, NY, USA

Correspondence: Kelly A. Balmes (kelly.balmes@noaa.gov)

Received: 1 June 2023 – Discussion started: 3 August 2023
Revised: 7 May 2024 – Accepted: 8 May 2024 – Published: 25 June 2024

Abstract. The Peak Design Ltd hyperspectral radiometer (HSR1) was tested at the Atmospheric Radiation Measurement (ARM) user facility Southern Great Plains (SGP) site in Lamont, Oklahoma, for 2 months from May to July 2022. The HSR1 is a prototype instrument that measures total (F_{total}) and diffuse (F_{diffuse}) spectral irradiance from 360 to 1100 nm with a spectral resolution of 3 nm. The HSR1 spectral irradiance measurements are compared to nearby collocated spectral radiometers, including two multifilter rotating shadowband radiometers (MFRSRs) and the Shortwave Array Spectroradiometer–Hemispheric (SASHe) radiometer. The F_{total} at 500 nm for the HSR1 compared to the MFRSRs has a mean (relative) difference of 0.01 W m^{-2} nm^{-1} (1 %–2 %). The HSR1 mean F_{diffuse} at 500 nm is smaller than the MFRSRs' by 0.03–0.04 (10 %) W m^{-2} nm^{-1}. The HSR1 clear-sky aerosol optical depth (AOD) is also retrieved by considering Langley regressions and compared to collocated instruments such as the Cimel sunphotometer (CSPHOT), MFRSRs, and SASHe. The mean HSR1 AOD at 500 nm is larger than the CSPHOT's by 0.010 (8 %) and larger than the MFRSRs' by 0.007–0.017 (6 %–18 %). In general, good agreement between the HSR1 and other instruments is found in terms of the F_{total}, F_{diffuse}, and AODs at 500 nm. The HSR1 quantities are also compared at other wavelengths to the collocated instruments. The comparisons are within $\sim$ 10 % for the F_{total} and F_{diffuse}, except for 940 nm, where there is relatively larger disagreement. The AOD comparisons are within $\sim$ 10 % at 415 and 440 nm; however, a relatively larger disagreement in the AOD comparison is found for higher wavelengths.

1 Introduction

The shortwave (SW) radiation reaching the surface is dependent on the radiation incident at the top of the atmosphere (TOA) and the aerosols, clouds, and other atmospheric constituents that scatter, absorb, and extinguish the incoming radiation as it passes through the atmosphere. The surface downwelling SW radiation varies spatially, temporally, and spectrally. By measuring the spectral SW radiation reaching the surface, insights into the physical, microphysical, and optical properties of aerosols and clouds are possible (Riihimaki et al., 2021).

Filter-based spectral SW radiation measurements have provided insight into the spectral characteristics of various atmospheric components by measuring at narrowband channels (Michalsky and Long, 2016; Riihimaki et al., 2021). For example, the multifilter rotating shadowband radiometers (MFRSRs) (Harrison et al., 1994; Harrison and Michalsky, 1994; Hodges and Michalsky, 2016) and Cimel sunphotome-

ter (CSPHOT) (Holben et al., 1998; Giles et al., 2019) have increased knowledge on aerosols (e.g., McComiskey and Ferrare, 2016), clouds (e.g., Michalsky and Long, 2016; Min et al., 2008; Wang and Min, 2008), water vapor (e.g., Turner et al., 2016; Michalsky et al., 1995), and trace gases (e.g., Alexandrov et al., 2002a, b). In tandem with the increasing need for further understanding of aerosols and clouds to inform weather, climate, and renewable energy forecasting, spectral SW radiation measurements have advanced and hyperspectral radiometers are more readily available. The Rotating Shadowband Spectrometer (RSS) (Harrison et al., 1999), Shortwave Array Spectroradiometer–Hemispheric (SASHe) (Flynn, 2016), and EKO MS-711 (García-Cabrera et al., 2020) are examples of existing hyperspectral radiometers. However, operations due to rotating shadowbands to measure the diffuse irradiance and calibrations of these instruments are challenging, as good solar alignment is needed for accurate measurements and moving parts have greater potential to fail in the field than stationary instrument components.

In an attempt to ease the operational difficulties of hyperspectral radiometry, a newly developed hyperspectral radiometer with no moving parts and no requirement for rotating shade rings or motorized solar tracking devices is now available, called the hyperspectral radiometer (HSR1) (Wood et al., 2017; Norgren et al., 2022). The HSR1 measures total (F_{total}) and diffuse (F_{diffuse}) spectral irradiance from 360 to 1100 nm with a spectral resolution of 3 nm. The HSR1 optical design is a development of the Sunshine Pyranometer (SPN1), which is a commercially available broadband radiometer (see Wood, 1999, and Badosa et al., 2014, for detailed descriptions). The HSR1 is operated by an embedded PC, which also includes measurements of internal pressure and humidity in the case, GPS position, and orientation, and the whole system is built into a rugged case (see Fig. 2 in Wood et al., 2017).

The HSR1 was designed with seven spectral sensors: six sensors placed on a hexagonal grid and one sensor at the center, under a complex static shading mask (see Fig. 1 in Badosa et al., 2014, and Wood et al., 2017). The shading mask design is to ensure that, at any time and for any location, (1) at least one sensor is always exposed to the full solar beam, (2) at least one sensor is always completely shaded, and (3) the solid angle of the shading mask is equal to π, thus corresponding to half of the hemispherical solid angle. With no moving parts or specific azimuthal alignment, the instrument is ideal for deployment on moving platforms such as ships and remote locations where regular maintenance is difficult.

Assuming isotropic diffuse sky radiance, the third property related to the shading mask implies that all sensors receive equal amounts (50 %) of F_{diffuse} from the rest of the sky hemisphere. Therefore, at any instant, the minimum signal (F_{min}) measured among the seven sensors is the shaded sensor, which measures half the F_{diffuse}, and the maximum signal (F_{max}) from among the seven sensors is fully exposed to the solar beam and, therefore, measures the direct irradiance (F_{direct}) plus half the F_{diffuse}. From this, the following relationships can be formed:

$$F_{\text{diffuse}} = 2F_{\text{min}}\,, \tag{1}$$

$$F_{\text{direct}} = (F_{\text{max}} - F_{\text{min}})\,, \tag{2}$$

$$F_{\text{total}} = F_{\text{direct}} + F_{\text{diffuse}} = F_{\text{max}} + F_{\text{min}}\,. \tag{3}$$

In the HSR1, F_{max} and F_{min} are selected from the integrated spectral measurements from each sensor, and these relationships are applied to the corresponding spectral measurements to calculate the F_{total} and F_{diffuse}. Due to the nature of the measurements, the F_{total} and F_{diffuse} are measured simultaneously and can be measured at a frequency of up to 1 Hz. This is in contrast to rotating shadowband systems, which must make the F_{total} and F_{diffuse} measurements in different positions of the shadowband rotation and, therefore, at different times in the operating cycle. The simultaneously measured HSR1 F_{total} and F_{diffuse} are similar to two nearby instruments measuring F_{total} and F_{diffuse} separately but simultaneously.

The spectrometer within the HSR1 is a significant improvement over those reported in Wood et al. (2017), which used either an array of low-cost commercial spectrometers or a fiber switch with a higher-specification spectrometer to measure the seven spectral inputs. The current HSR1 uses a custom-designed multichannel spectrometer, which images and spectrally disperses the solar radiation from the input fibers onto a 2D image sensor, so all channels are measured simultaneously. This significantly improves the measurement resolution, speed, and matching between the channels compared with the earlier implementations. An early version of this system was also used by Norgren et al. (2022).

In this study, the prototype HSR1 is evaluated. The HSR1 was at the Atmospheric Radiation Measurement (ARM) user facility Southern Great Plains (SGP) site in Lamont, Oklahoma, for a 2-month test period from May to July 2022. The ARM SGP site is an ideal location to evaluate a new instrument, with the collocation of several instruments making similar measurements as a reference to compare with. The reference instruments include two MFRSRs, a CSPHOT, and a SASHe utilized to evaluate the HSR1's ability to measure F_{total} and F_{diffuse} as well as retrieve aerosol optical depth (AOD).

Section 2 describes the HSR1 data and general performance as well as other instruments and data sources utilized in the evaluation. Section 3 details the HSR1 AOD retrieval methodology. Section 4 presents the results of the HSR1 comparison. Section 5 briefly discusses postprocessing modifications and calibration checks and the resultant implication for the HSR1 data and evaluation results. Section 6 presents concluding remarks.

2 Data

2.1 HSR1

The HSR1 prototype was at the ARM SGP site in Lamont, Oklahoma (36.61° N, 97.49° W), from 16 May to 18 July 2022 for the test period. The HSR1 was located in the guest instrument facility (GIF) at the Central Facility (C1) (Fig. 1). The HSR1 exhibited excellent uptime and near-autonomous data collection over the 2-month test period, with an uptime of 97.5 %. The HSR1 time period sets the time period for the rest of the study. Other measurements (Sect. 2.2) are considered temporally collocated to the HSR1 when observations are within 1 min. A map showing the spatial distribution of the other instruments is shown in Fig. 1, with all the instruments separated by 170 m or less.

The HSR1 spectrometer achieves an optical resolution of 3 nm over the range 350 to 1050 nm and can take a measurement in as little as 200 ms. However, to improve the dynamic range of the instrument over the spectral range and also capture the range of diurnal irradiances, readings are taken over a series of different integration times and merged into a single high-dynamic-range measurement. This typically gives a measurement time of around 1 s. There is a tradeoff between speed and dynamic range. In this study, measurements were made every 10 s and then averaged and stored every minute to match common solar radiation datasets.

Example time series for HSR1-integrated irradiance and example spectra from 11 July 2022 are shown in Fig. 2. The integrated irradiances are the spectral irradiances integrated from 400 to 1000 nm. On this day, the conditions were primarily clear-sky. Other features of note in the time series and spectra from this day will be described throughout the remainder of this section.

Several features of the HSR1 performance were noted. The general excellent HSR1 performance is further described in the later sections as the main focus of this study. Here, the limited performance issues are described. The data exhibited measurement noise due to straylight issues for wavelengths less than 400 nm and for wavelengths greater than 950 nm. In particular, considerable noise was noted for wavelengths greater than 1000 nm (Fig. 2c) as the measurements were contaminated by second-order straylight as identified in the lab using a monochromator. As with all spectrometers, measurements at the two edges of the spectrum have low sensitivity and, therefore, additional noise is apparent. Due to the measurement noise, this comparison study focuses on the spectral range of 400 to 950 nm.

In addition to straylight issues, the data exhibited step functions throughout the diurnal cycle (Fig. 2a). This phenomenon is partially due to the shading mask pattern design as the measurement switches between the seven sensors as the sun angle changes throughout the day. By utilizing seven sensors instead of one sensor, this introduces different calibration errors across the sensors that lead to the step functions. The HSR1 dome also contributes to this issue as the incoming light is bent due to the dome's refracting properties, which is referred to as the dome lensing effect (Badosa et al., 2014). The dome lensing effect can be corrected for by a set of equations that take into account the geometry of the solar position and the HSR1 and the resultant change in the angle of the incoming light as the light passes through the dome into the sensors. The F_{total} and F_{diffuse} corrected for the dome lensing effect are discussed further in Sect. 5. These corrections will also be the subject of a future study, as noted in Sect. 5.

Furthermore, the cosine response of the seven sensor diffusers is measured in the lab using a collimated beam from a xenon lamp and is within 2 % of the normal beam irradiance

Figure 1. Map (from © Google Earth) of the instruments at the ARM SGP site. The HSR1 is indicated by a red marker, and all the other instruments are shown with an orange marker. The instrument names are labeled near their respective markers. The yellow line indicates a distance of 170 m for scale.

Table 1. Instrument specifications, including spectral range, spectral resolution, retrieved quantities, and uncertainty estimates.

Instrument	Measurement	Spectral coverage (resolution)	Retrieved quantities	Uncertainty estimates
HSR1	Total and diffuse hyperspectral irradiances	360–1100 nm (3 nm)	AOD at 415, 440, 500, 615, 673, 675, and 870 nm	Total irradiances: 5 % AOD: 0.02
CSPHOT	Direct solar irradiance and sky radiance	340, 380, 440, 500, 675, 870, 1020, and 1640 nm	AOD at 440, 500, 675, and 870 nm	AOD: 0.01
MFRSR	Total and diffuse spectral narrowband irradiances	415, 500, 615, 673, 870, and 940 nm	AOD at 415, 500, 615, 673, and 870 nm	Irradiances: 3 % AOD: 0.01
SASHe	Total and diffuse hyperspectral irradiances	336 to 1100 nm ($\sim$ 2.5 nm), 950 to 1700 nm (6 nm)	AOD at 415, 500, 615, 673, and 870 nm	AOD: 0.02–0.03 Irradiances: AOD relative uncertainty multiplied by the air mass

over the range of zenith angles. The cosine response curves for the HSR1 in this study are shown in Fig. 3.

2.1.1 Calibration and uncertainty

A reference HSR1 is calibrated by removing the shading mask and exposing the sensors to a 1000 W "FEL" lamp, with an output spectrum calibrated by the UK National Physical Laboratory (NPL). This enables identical calibration of the seven sensors to direct beam light. The same sensitivity applies to diffuse light, though it is modified by the geometry of the shading mask (Eq. 1).

This calibration is transferred to other HSR1s during routine calibrations and calibration checks using an integrating sphere. The expected uncertainty in F_{total} measurements is expected to be around 5 % between 400 and 900 nm.

2.1.2 Field of view (FOV)

As described in Badosa et al. (2014), the HSR1 optical system has a larger FOV than a typical sun photometer. The precise FOV is somewhat variable, depending on the position of the sun in the sky, but it is typically around $\pm 7°$. This means that the circumsolar irradiance will normally be included as part of the F_{direct} rather than in the F_{diffuse}, as would be the case with a narrow FOV sun photometer. This means that the HSR1 F_{diffuse} measurement will typically be lower than the corresponding measurements from a sun photometer or broadband tracker system. An analysis by Norgren et al. (2022) (see their Appendix A) quantified this for the case of thin clouds, estimating a circumsolar irradiance varying between negligible and ~ 10 % of the direct beam, depending on solar zenith angle and cloud thickness. Implementing a correction for this will be a topic for further study.

2.2 Other data

2.2.1 CSPHOT

The CSPHOT AODs are considered in the comparison (Holben et al., 1998). The CSPHOT observations are from the AErosol RObotic NETwork (AERONET) Version 3 Level-2 AOD data product, which provides quality-assured and filtered AODs under clear-sky conditions (Giles et al., 2019). The CSPHOT observations considered include the AODs at 440, 500, 675, and 870 nm wavelengths. The AERONET AOD uncertainty is 0.01 for the wavelengths considered in this study (Giles et al., 2019).

2.2.2 MFRSRs

The MFRSR measures narrowband F_{total} and F_{diffuse} at 415, 500, 615, 673, 870, and 940 nm wavelengths (Harrison et al., 1994; Harrison and Michalsky, 1994; Hodges and Michalsky, 2016). Two MFRSRs were collocated to the HSR1 with facility designations C1 and E13. The MFRSR narrowband filters measure with a nominal central wavelength at each desired wavelength and a nominal full width half maximum (FWHM) of 10 nm. The central wavelength and FWHM are measured for each narrowband channel to determine the transmission characteristics of each specific instrument. For example, the MFRSR C1-measured characteristics for the 500 nm channel include a central wavelength of 501.5 nm and a FWHM of 10.7 nm. The estimated uncertainty in the spectral irradiances is 3 %, which is based on the estimated uncertainty of the RSS that follows the exact same shadowing method (Michalsky and Kiedron, 2022).

In addition to the spectral irradiances, MFRSR-retrieved AODs are also considered at 415, 500, 615, 673, and 870 nm wavelengths with an estimated uncertainty of 0.01 (Koontz et al., 2013).

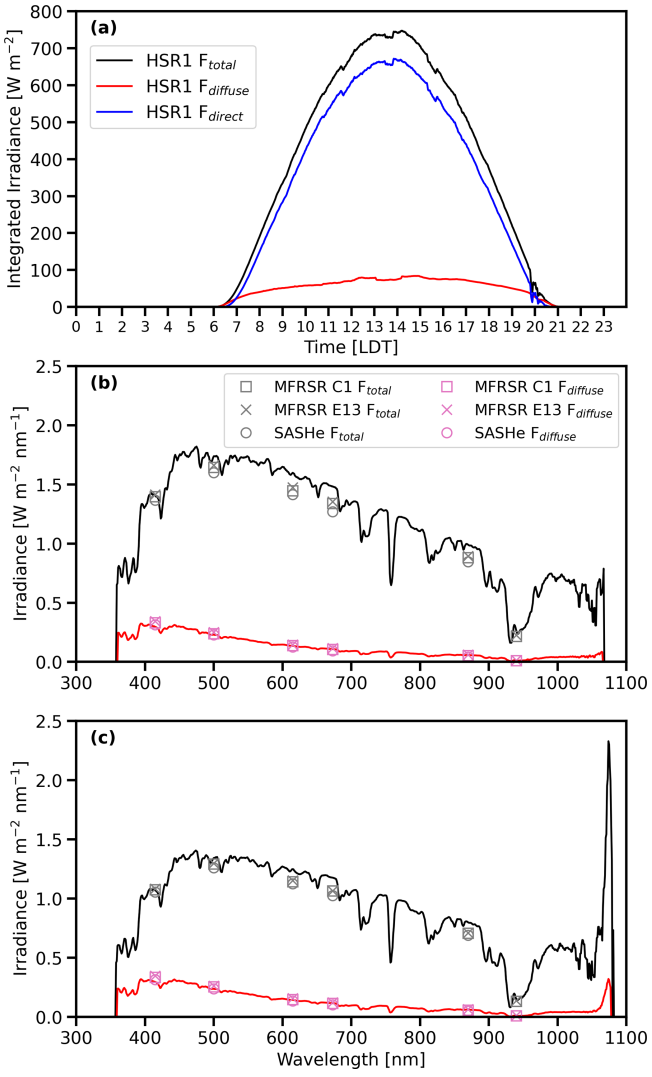

Figure 2. **(a)** HSR1 time series, in local daylight time (LDT), of integrated irradiance for F_{total} (black), F_{diffuse} (red), and F_{direct} (F_{total}–F_{diffuse}) (blue) irradiances from 11 July 2022. HSR1 spectra are from the same date at **(b)** 13:53 LDT and **(c)** 16:28 LDT. Collocated F_{total} (gray) and F_{diffuse} (pink) from the MFRSR C1 (square), MFRSR E13 (x mark), and SASHe (circle) are also shown.

2.2.3 SASHe

The SASHe measures F_{total} and F_{diffuse} from 336 to 1700 nm (Flynn, 2016), although there are wavelength regions where absorbing gas features hinder radiometric calibration and thus limit the usefulness of the measurement. The spectral resolution of the SASHe is about 2.5 nm for the spectral range where the SASHe and HSR1 overlap. During the course of this study, two instrument issues were identified that affected the operation of the SASHe and the quality of the reported data, which limited the data to clear-sky conditions only (see Appendix A). Thus, the SASHe clear-sky F_{total}, F_{diffuse}, and AODs at 415, 500, 615, 673, and 870 nm wavelengths are compared to the other instruments.

Due to the data quality issues mentioned above, the SASHe irradiance and AOD uncertainties are difficult to quantify. The uncertainty in AOD is likely not less than 0.02–0.03. The SASHe irradiances are not directly calibrated. Instead, they are derived from Langley calibration (see Appendix A), where the retrieved TOA spectral irradiance is scaled to agree with those in MODTRAN. Therefore, the uncertainty in the irradiance components and the AOD are directly related. Specifically, the irradiance relative uncertainty will be equal to the relative AOD uncertainty multiplied by the air-mass value.

2.2.4 Radiative Flux Analysis (RADFLUX) data product

RADFLUX utilizes quality-controlled broadband surface downwelling total ($F_{\text{broadband, total}}$) and diffuse ($F_{\text{broadband, diffuse}}$) SW irradiance observations to identify clear-sky periods and then calculate clear-sky irradiances (Long and Ackerman, 2000; Long et al., 2006; Riihimaki et al., 2019). The SW broadband radiometer spectral range is 295 to 3000 nm (Andreas et al., 2018). The estimated uncertainties are 4 % in $F_{\text{broadband, total}}$ and 3 % in $F_{\text{broadband, diffuse}}$ (Michalsky and Long, 2016).

RADFLUX processing first identifies clear-sky time periods using the magnitude and variability of the diffuse and total SW irradiance that have been normalized to remove the impacts of the diurnal cycle. Clear-sky estimates are determined at all times using empirical fits to those data points (Long and Ackerman, 2000). Finally, cloud fraction (CF) is calculated based on a relationship with the normalized diffuse cloud effect (i.e., (diffuse measured − diffuse clear sky) / total clear sky). Care is taken to distinguish between optically thin and thick clouds in the CF calculations using statistics on the magnitude and variability of the irradiance measurements and the diffuse ratio (see Long et al., 2006, for more details).

In this study, the clear-sky identified time periods from RADFLUX are considered for the AOD retrieval (Sect. 3) based on when the SW CF is equal to 0. The SW CF uncertainty is 10 % (Long et al., 2006). In addition, the broadband diffuse ratio (i.e., $F_{\text{broadband, diffuse}}/F_{\text{broadband, total}}$) from RADFLUX is compared to that from the HSR1. The RADFLUX data product considered in this study has the facility designation E13.

2.2.5 Ozone Monitoring Instrument (OMI)

The ozone column amount for the AOD retrieval is from the OMI on board the Aura satellite (Levelt et al., 2018). Global coverage at a spatial resolution of 1° latitude by 1° longitude of daily ozone values from the OMI is provided in the gecomiX1.a1 data product. The daily ozone value corre-

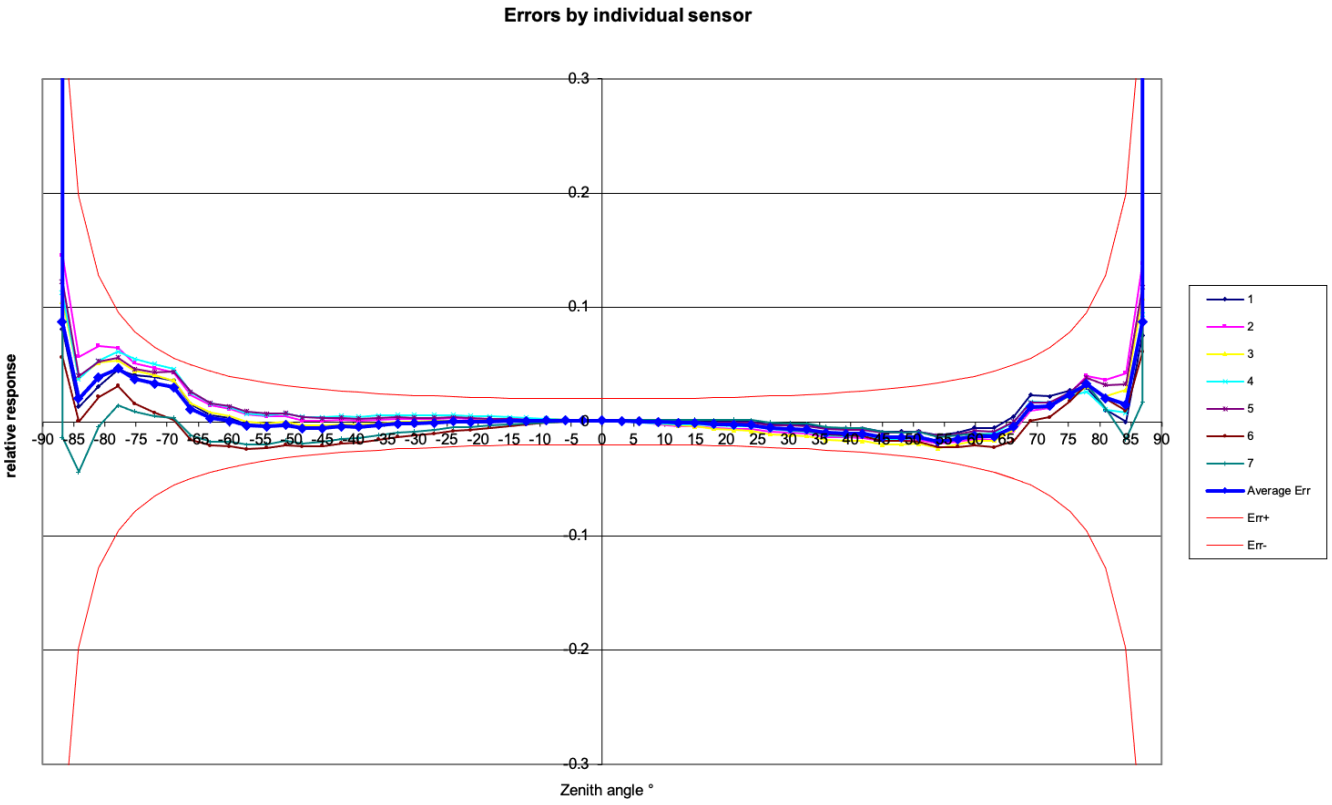

Figure 3. Cosine curve for the seven sensors of the HSR1. The heavy blue line shows an average of these, and the red lines show 2 % design limits.

sponding to the SGP's latitude and longitude are considered in the HSR1 AOD retrieval (Sect. 3).

3 AOD retrieval

The HSR1 AOD is retrieved by considering Langley regressions. The HSR1 AOD retrieval is based on the AOD retrieval methodologies of the MFRSR (Koontz et al., 2013) and SASHe (Ermold et al., 2013). Only clear-sky periods are considered, which are based on the RADFLUX SW CF (Sect. 2.2.4). The AODs are found for wavelengths with the corresponding CSPHOT- and MFRSR-retrieved AODs: 415, 440, 500, 615, 673, 675, and 870 nm.

For a clear-sky atmosphere (i.e., no clouds), the spectral direct normal irradiance (DNI) at a given wavelength (λ) that reaches the surface can be described as

$$\mathrm{DNI}(\lambda) = \mathrm{DNI}_0(\lambda) \exp \left[-\left(\tau_{\mathrm{Rayleigh}}(\lambda) + \tau_{\mathrm{aerosol}}(\lambda) + \tau_{\mathrm{gas}}(\lambda) \right) m \right], \quad (4)$$

where DNI_0 is the DNI at the top of the atmosphere (TOA), τ_{Rayleigh} is the Rayleigh optical depth due to molecular scattering, τ_{aerosol} is the AOD, τ_{gas} is the gaseous absorption optical depth, and m is the air mass. By considering the gaseous absorption to be linearly proportional to the air mass and taking the natural logarithm, Eq. (2) becomes

$$\ln(\mathrm{DNI}(\lambda)) = \ln(\mathrm{DNI}_0(\lambda)) - \left(\tau_{\mathrm{Rayleigh}}(\lambda) + \tau_{\mathrm{aerosol}}(\lambda) + \tau_{\mathrm{gas}}(\lambda) \right) m . \quad (5)$$

By linearly regressing the HSR1 spectral DNI and air mass, the TOA DNI (from the y intercept) and the total optical depth (from the slope) can be found.

Besides DNI and AOD, the other terms in Eq. (3) are calculated as follows. The Rayleigh optical depth is calculated as (Hansen and Travis, 1974)

$$\tau_{\mathrm{Rayleigh}} = \frac{p}{1013.25} 0.008569 \lambda^{-4} \left(1 + 0.0133 \lambda^{-2} + 0.00013 \lambda^{-4} \right), \quad (6)$$

where p is the surface pressure (mbar) and λ is the wavelength (µm). The surface pressure considered is from RADFLUX. The air mass is calculated as (Kasten and Young, 1989)

$$m = \frac{1}{\cos(\theta_s) + 0.50572 (96.07995 - \theta_s)^{-1.6364}}, \quad (7)$$

where θ_s is the solar zenith angle (°).

For τ_{gas}, only the effect of ozone is considered due to the wavelengths considered as other gaseous absorption is considered negligible (Koontz et al., 2013; Ermold et al., 2013).

In addition, only the column amount of ozone is considered (i.e., no vertical dependence). The ozone optical depth, τ_{ozone}, is calculated as

$$\tau_{\text{ozone}}(\lambda) = \frac{\text{ozone columnar amount}}{1000} \cdot A_{\text{ozone}}(\lambda), \quad (8)$$

where ozone columnar amount is the total amount of ozone in the atmospheric column in Dobson units and A_{ozone} is the spectrally dependent ozone gas absorption coefficient. The ozone columnar amounts are from the daily ozone satellite value (Sect. 2.2.5) and are closest in time, and the absorption coefficients are from Ermold et al. (2013) (see their Appendix A). Note that water vapor is not included in τ_{gas} due to the wavelengths considered, which apart from 940 nm (not included in the AOD retrieval) have a negligible amount of water vapor absorption.

Langley regressions are found each day for two periods: morning and afternoon. The minimum in air mass (i.e., solar noon) separates each day's clear-sky times into morning and afternoon. The TOA DNIs are then filtered by only considering the interquartile range (i.e., 25th–75th percentiles) to eliminate outliers and reduce noise (Koontz et al., 2013; Ermold et al., 2013). The filtered TOA DNIs are smoothed using a Savitzky–Golay filter. The filtered and smoothed TOA DNI values for each wavelength considered are then utilized to retrieve the spectral HSR1 AOD for each clear-sky time.

The HSR1 AOD uncertainty is quantified. Since the HSR1 AOD is retrieved from Langley regressions, the AOD uncertainty is independent of the HSR1 irradiance calibration. The HSR1 AOD uncertainties are due to (1) uncertainties in the TOA DNI, (2) cosine errors, and (3) dome lensing effects. The TOA DNI uncertainty is 1 %, as determined by the standard error of the means. The cosine error uncertainty is 2 %, based on instrument design limits. The dome lensing effect uncertainty is 1 %, as calculated from optical theory. The HSR1 AOD uncertainty is determined by considering the perturbation of the HSR1 AOD to the uncertainty sources. The resultant perturbation to the HSR1 AOD is ± 0.02.

4 Results

4.1 Irradiance comparison

Time series of the HSR1 F_{total} and F_{diffuse} at 500 nm and the MFRSR C1 F_{total} and F_{diffuse} at 500 nm are shown in Fig. 4. The HSR1 F_{total} and F_{diffuse} were collocated and compared to those from the MFRSR C1 and MFRSR E13. The resultant comparisons of the F_{total} at 500 nm are shown in Fig. 5, the F_{diffuse} at 500 nm in Fig. 6, and the F_{total} and F_{diffuse} for all MFRSR wavelengths in Fig. 7. The MFRSR C1 and MFRSR E13 spectral irradiances are also compared to each other in Figs. 5–7 to provide context to the HSR1 comparison by showing the level of agreement between two instruments of the same model at the same location. In addition, the regression lines and the regression lines of the bias are shown in Figs. 5 and 6, which provide additional information on how the bias changes across different modes. The regression lines of the bias are constructed by regressing the bias (e.g., instrument 2 − instrument 1) with the reference instrument values (e.g., instrument 1).

4.1.1 Irradiance at 500 nm comparison

In general, the HSR1 F_{total} at 500 nm is slightly larger than those from both MFRSRs, with small mean (relative) differences at 500 nm of $\sim 0.01\,\text{W m}^{-2}\,\text{nm}^{-1}$ (1 %–2 %). The small mean differences, large correlation coefficients, regression slopes near 1, and bias regression slopes near 0 demonstrate excellent agreement between the HSR1 and the two MFRSRs in terms of the F_{total} at 500 nm (Fig. 5). Furthermore, the HSR1 F_{total} at 500 nm is within the MFRSR uncertainty (3 %; Table 1) of the MFRSR F_{total} at 500 nm for 45.0 % (MFRSR C1) and 54.8 % (MFRSR E13) of the time.

The HSR1 F_{diffuse} is ~ 10 % smaller than those from both MFRSRs, which may be partially related to the instrument design in how the HSR1 measures the F_{diffuse}, as noted previously (Badosa et al., 2014). This includes the isotropic assumption and the HSR1's wider FOV compared to the other instruments. In reality, some of the forward-scattered circumsolar radiation is included in the HSR1 F_{direct}, which would be measured as F_{diffuse} by instruments with a narrower FOV. This explains much of the underestimation of F_{diffuse} observed in this comparison study. The overall impact is a -0.03 to $0.04\,\text{W m}^{-2}\,\text{nm}^{-1}$ mean difference, with negative bias regression slopes of ~ -0.16 as shown in Fig. 6. As a result, the HSR1 F_{diffuse} at 500 nm is within the MFRSR uncertainty of the MFRSR F_{diffuse} at 500 nm only 10.6 % (MFRSR C1) and 7.3 % (MFRSR E13) of the time.

By comparison, the MFRSR C1 and MFRSR E13 were also compared in terms of the F_{total} and F_{diffuse} at 500 nm and found to agree well. The mean (relative) differences in the F_{total} and F_{diffuse} are $0.005\,\text{W m}^{-2}\,\text{nm}^{-1}$ (0.5 %) and $0.003\,\text{W m}^{-2}\,\text{nm}^{-1}$ (0.9 %), respectively. The F_{total} and F_{diffuse} correlation coefficients and regression slopes are near 1, with bias regression slopes of near 0. The F_{total} and F_{diffuse} of the MFRSRs are within the MFRSR uncertainty of each other for 80.2 % and 82.7 % of the time, respectively. The comparison of the spectral irradiances between the two MFRSRs with the same instrument design and same data processing quantifies some of the uncertainty. It is also encouraging for the HSR1 that, with an independent instrument design and data processing, the HSR1 spectral irradiances agree well with those from the MFRSRs.

4.1.2 Irradiance at MFRSR wavelength comparison

Figure 7 extends the comparison between the HSR1 and the MFRSR irradiance to the additional MFRSR wavelengths (i.e., 415, 615, 673, 870, and 940 nm). For the F_{total}, the relative orderings of the comparison results are similar to those

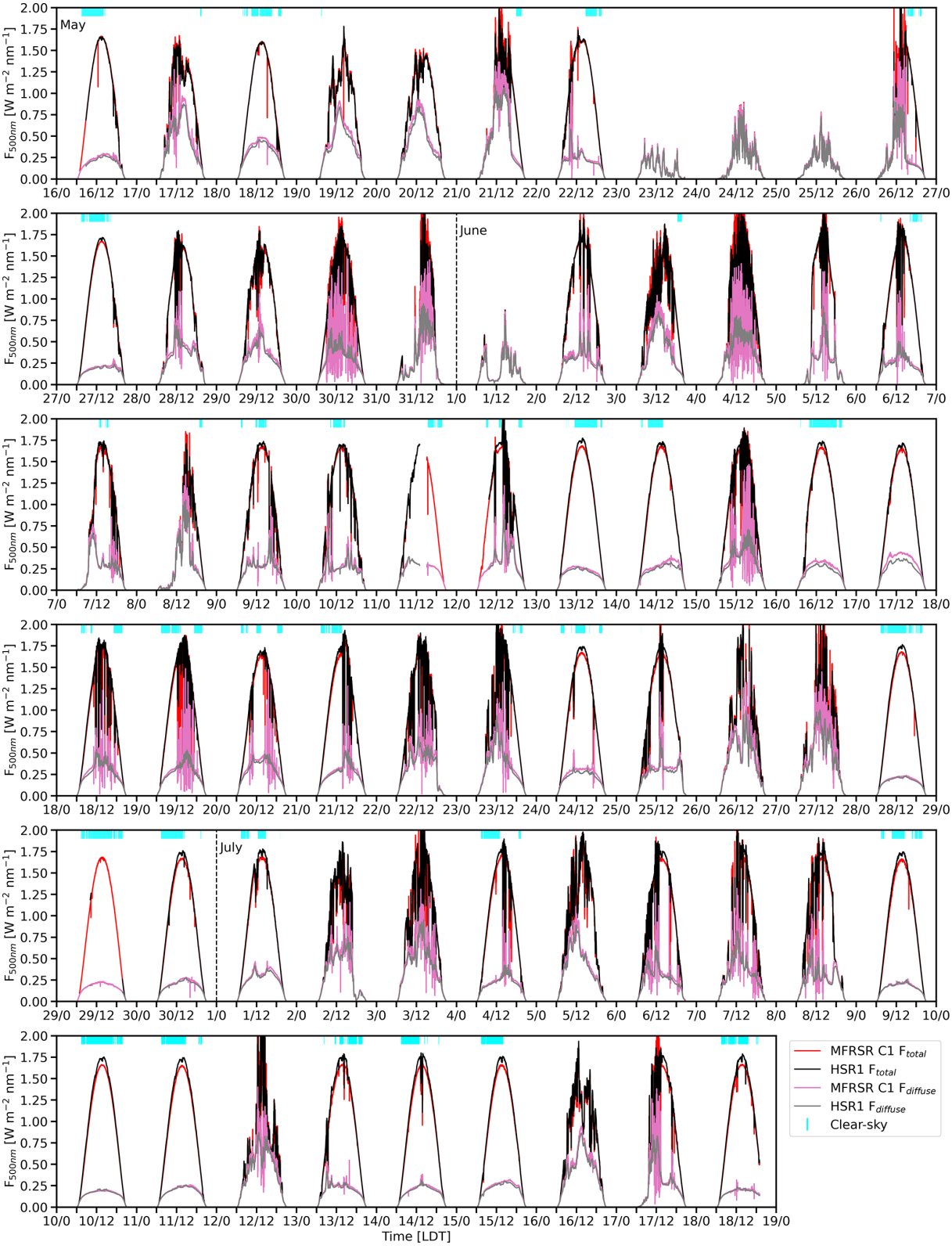

Figure 4. Time series (LDT) of the F_{total} and F_{diffuse} at 500 nm (W m^{-2} nm^{-1}). The MFRSR C1 F_{total} (red), HSR1 F_{total} (black), MFRSR C1 F_{diffuse} (pink), and HSR1 F_{diffuse} (gray) are shown. The light-blue vertical lines indicate clear-sky periods. The dashed vertical black lines indicate the start of each month, and the x-axis tick marks indicate the day and hour.

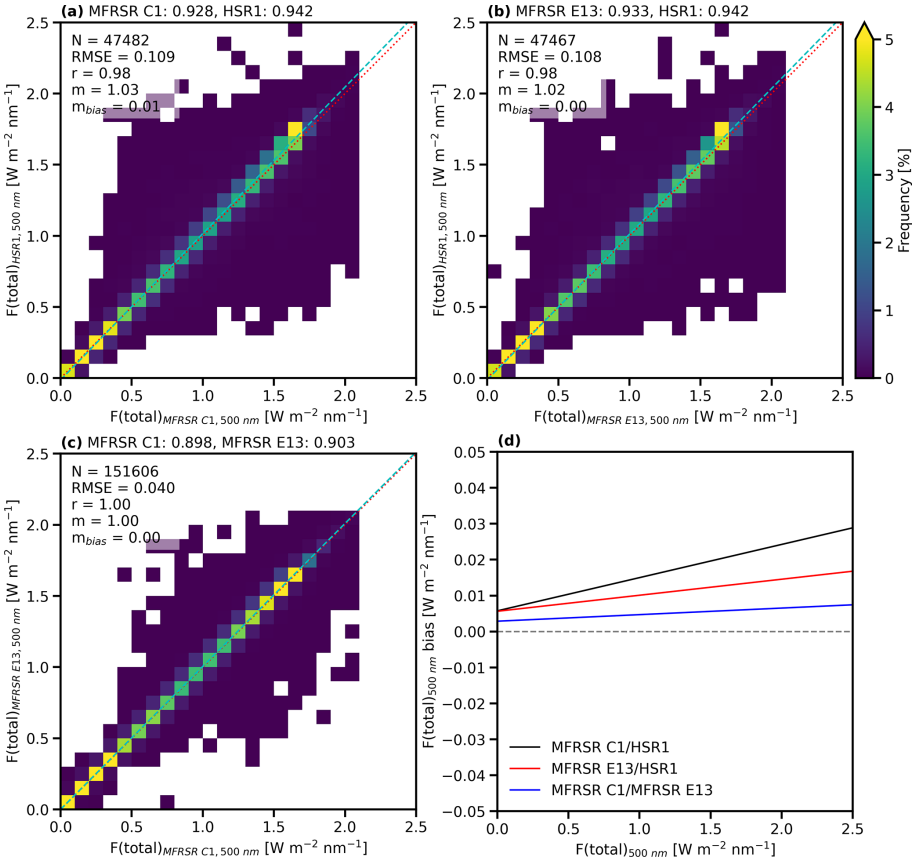

Figure 5. Frequency histogram for F_{total} at 500 nm (W m^{-2} nm^{-1}) of collocated **(a)** MFRSR C1 and HSR1, **(b)** MFRSR E13 and HSR1, and **(c)** MFRSR C1 and MFRSR E13. The mean values are given above each plot. The sample size (N), root mean squared error (RMSE), correlation coefficient (r), regression line slope (m), and bias regression line slope (m_{bias}) are shown in the top left of each plot. The 1 : 1 line is indicated by the dotted red line, and the regression line is indicated by the dashed light-blue line. **(d)** The regression lines of the bias are shown for MFRSR C1 and HSR1 (black), MFRSR E13 and HSR1 (red), and MFRSR C1 and MFRSR E13 (blue). The zero line is indicated by the dashed gray line.

at 500 nm (Fig. 5): the mean HSR1 F_{total} is slightly larger than those from the MFRSRs. The exception is at 415 nm, where the HSR1 F_{total} is slightly smaller than those from the MFRSRs by 2 %–3 %. The relative differences in F_{total} between the HSR1 and the MFRSRs are 8 % or less, except at 940 nm. Similar to the comparison at 500 nm, the HSR1 F_{total} at 415 nm was within the MFRSR uncertainty of the MFRSRs for 50 % of the time. For 615–870 nm, the HSR1 F_{total} was within the MFRSR uncertainty of the MFRSRs for 15 %–22 % of the time. The HSR1 F_{total} RMSE compared to the MFRSRs increases with wavelength until it reaches its largest value at 615 nm, and then the HSR1 F_{total} RMSE decreases with wavelength (Fig. 7d).

At 940 nm, the HSR1 mean F_{total} is larger than the MFRSRs by 16 %–21 %. Furthermore, the HSR1 F_{total} was within the MFRSR uncertainty of the MFRSRs only 5 %–7 % of the time. The larger relative difference is partially due to the small magnitude of the mean F_{total} at 940 nm of ~ 0.1 W m^{-2} nm^{-1}, noting that the mean differences are ~ 0.02 W m^{-2} nm^{-1}. For reference, the MFRSR C1 and MFRSR E13 F_{total} comparison at 940 nm is the largest relative difference spectrally as well with 4.5 %, which is considerably higher than other wavelengths (0.3 % to 1.0 %). This highlights the difficult and highly variable nature of measuring the F_{total} at 940 nm, where water vapor absorption is strong (Michalsky et al., 1995).

The F_{diffuse} comparison at all the MFRSR wavelengths follows a similar pattern in a relative difference sense to the comparison at 500 nm (Fig. 6): the HSR1 F_{diffuse} are smaller than those from both the MFRSRs at all MFRSR wavelengths by ~ 4 %–14 %. The relative differences range from -3.7 % for the HSR1 F_{diffuse} compared to those from the MFRSR C1 at 940 nm to -13.5 % for the HSR1 F_{diffuse} compared to those from the MFRSR E13 at 415 nm. The HSR1 F_{diffuse} were within the MFRSR uncertainty only 2 % of the time at 415 nm but 15 %–25 % of the time at 615–870 nm. The HSR1 F_{diffuse} RMSE compared to the MFRSRs decreases with increasing wavelength, which is a similar

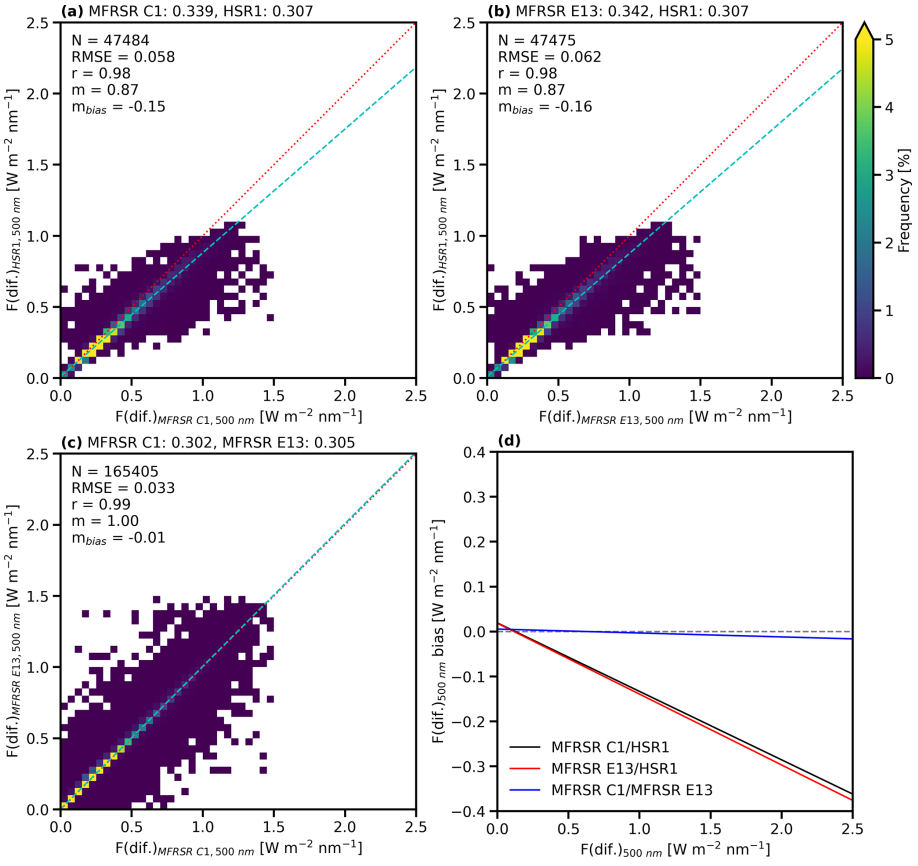

Figure 6. The same as Fig. 5 but for F_{diffuse} at 500 nm.

spectral dependence to the F_{diffuse} RMSE between the two MFRSRs (Fig. 7d).

Interestingly, the mean F_{diffuse} for the HSR1 compared to those from the MFRSR C1 at 940 nm agree better than the MFRSR C1 and MFRSR E13 F_{diffuse} at 940 nm, with a relative difference of 9.8 %. However, the mean differences for the F_{diffuse} at 940 nm are small in magnitude, at only 0.002 W m^{-2} nm^{-1}. Similar to the F_{total} comparison, the MFRSR C1 and MFRSR E13 F_{diffuse} relative difference is largest at 940 nm compared to the relative differences at other MFRSR wavelengths. For context, the relative difference at 940 nm is nearly 1 order of magnitude larger than all the other wavelengths ($\sim$ 1.4 %). In addition, the HSR1 F_{diffuse} at 940 nm was within the MFRSR uncertainty of the MFRSRs by the same amount or more so (5 %–12 %) than the MFRSRs were with each other (5.4 %). This further highlights the challenges in measuring the spectral irradiance at 940 nm as two of the same instruments in the same location differ the most in this channel.

The impacts of the MFRSR narrowband filter on the comparison results were quantified by considering the HSR1 spectra weighted by the MFRSR transmission spectra. In general, the HSR1 mean spectral irradiances decreased, with the mean F_{total} decreasing by 0.012 W m^{-2} nm^{-1} or less and the mean F_{diffuse} decreasing by 0.005 W m^{-2} nm^{-1} or less. This resulted in the mean F_{total} comparison between the HSR1 and the two MFRSRs improving by 1.0 % or less, except at 940 nm ($\sim$ 2.5 %) and 415 nm (~ -1.3). For the mean F_{diffuse}, the comparison worsened by 1.5 % or less, except at 940 nm (~ -3.5 %). Overall, the impact of the MFRSR narrowband filter on the results is minimal, with changes in the HSR1 spectral irradiances and resultant comparison of $\sim$ 0.01 W m^{-2} nm^{-1} ($\sim$ 1.5 %) or less on average.

4.1.3 SASHe clear-sky irradiance comparison

The HSR1 F_{total} and F_{diffuse} were compared to the SASHe clear-sky irradiances. The SASHe clear-sky irradiances were also compared to the two MFRSRs. The resultant comparisons for the F_{total} and F_{diffuse} are shown in Fig. 8.

Detailed comparisons of the F_{total} at 500 nm (Fig. 8a) show that the mean (relative) difference for the HSR1 F_{total} compared to those from the SASHe is 0.017 W m^{-2} nm^{-1} (1.5 %). The SASHe F_{total} were also compared to those from the two MFRSRs (Fig. 8b and c), showing mean (relative) differences of $\sim$ 0.003 W m^{-2} nm^{-1} (0.3 %). The regression slopes are less than 1 and the bias regression slopes are negative, which is due to low-biased SASHe F_{total} values at

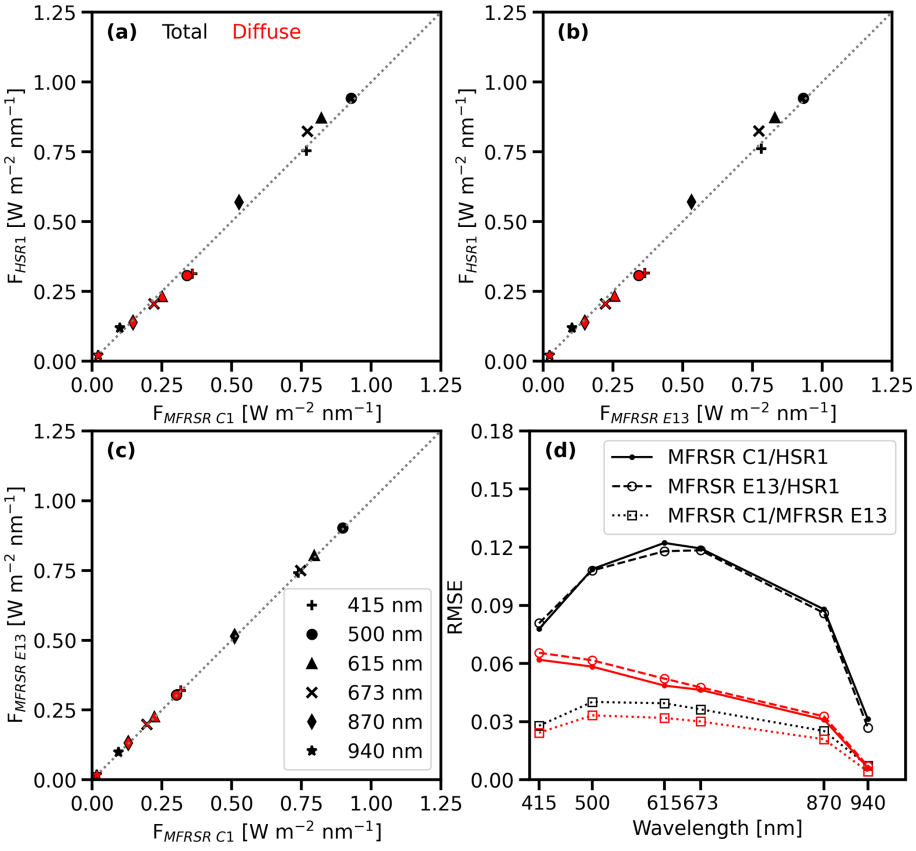

Figure 7. Mean F_{total} (black) and F_{diffuse} (red) ($\text{W m}^{-2}\,\text{nm}^{-1}$) of collocated **(a)** MFRSR C1 and HSR1, **(b)** MFRSR E13 and HSR1, and **(c)** MFRSR C1 and MFRSR E13. The wavelengths considered include 415 nm (plus sign), 500 nm (circle), 615 nm (triangle), 673 nm (x mark), 870 nm (diamond), and 940 nm (star). The 1 : 1 line is indicated by the dotted gray line. **(d)** RMSEs are shown for F_{total} (black) and F_{diffuse} (red) for MFRSR C1 and HSR1 (solid line with dot), MFRSR E13 and HSR1 (dashed line with open circle), and MFRSR C1 and MFRSR E13 (dotted line with square).

larger irradiances ($>\approx 1.5\,\text{W m}^{-2}\,\text{nm}^{-1}$). The SASHe F_{total} at 500 nm is within the MFRSR uncertainty of the MFRSR F_{total} at 500 nm for 67 %–72 % of the time.

Similar to the HSR1 comparison in Fig. 6, the HSR1 F_{diffuse} is smaller than that from the SASHe. For the F_{diffuse} at 500 nm, the mean (relative) difference for the HSR1 F_{diffuse} compared to those from the SASHe is $-0.019\,\text{W m}^{-2}\,\text{nm}^{-1}$ (-6.4 %). The SASHe F_{diffuse} is slightly smaller than those from the MFRSRs by $-0.009\,\text{W m}^{-2}\,\text{nm}^{-1}$ (~ -3 %). The SASHe F_{diffuse} at 500 nm is within the MFRSR uncertainty of the MFRSR F_{diffuse} at 500 nm for 44 %–53 % of the time.

A summary of comparisons of the mean F_{total} and F_{diffuse} irradiances at multiple wavelengths is shown between the SASHe and HSR1 (Fig. 8i), MFRSR C1 (Fig. 8j), and MFRSR E13 (Fig. 8k). The SASHe and HSR1 mean F_{total} comparisons are similar to those at 500 nm as the HSR1 F_{total} is typically slightly larger than those from the SASHe by $0.08\,\text{W m}^{-2}\,\text{nm}^{-1}$ (9 %) or less, except at 415 nm, where the HSR1 F_{total} is smaller by $0.01\,\text{W m}^{-2}\,\text{nm}^{-1}$ (1.5 %). The SASHe mean F_{total} compared to those from the two MFRSRs agree within 2 % or less for all wavelengths. The SASHe F_{total} are within the MFRSR uncertainty of the MFRSRs for 48 %–76 % of the time. For the mean F_{diffuse}, the HSR1 F_{diffuse} is smaller than those from the SASHe by $0.03\,\text{W m}^{-2}\,\text{nm}^{-1}$ (9 %) or less. The SASHe mean F_{diffuse} compared to those from the MFRSRs are smaller by $0.02\,\text{W m}^{-2}\,\text{nm}^{-1}$ or less. This corresponds to within 8 % or less. The SASHe F_{diffuse} are within the MFRSR uncertainty of the MFRSRs for 19 %–42 % of the time.

4.2 AOD comparison

The HSR1 clear-sky AODs were compared to those from the CSPHOT, the MFRSRs, and the SASHe. The resultant comparison of the AODs at 500 nm is shown in Fig. 9, and for the AODs at all overlapping wavelengths (i.e., 415, 440, 500, 615, 673, 675, and 870 nm), it is shown in Fig. 10. The HSR1 AOD at 500 nm shows relative differences between 6 % and 18 % compared with retrievals from the other instruments. In general, the HSR1 AOD is larger than those from the other instruments, except for the SASHe AOD.

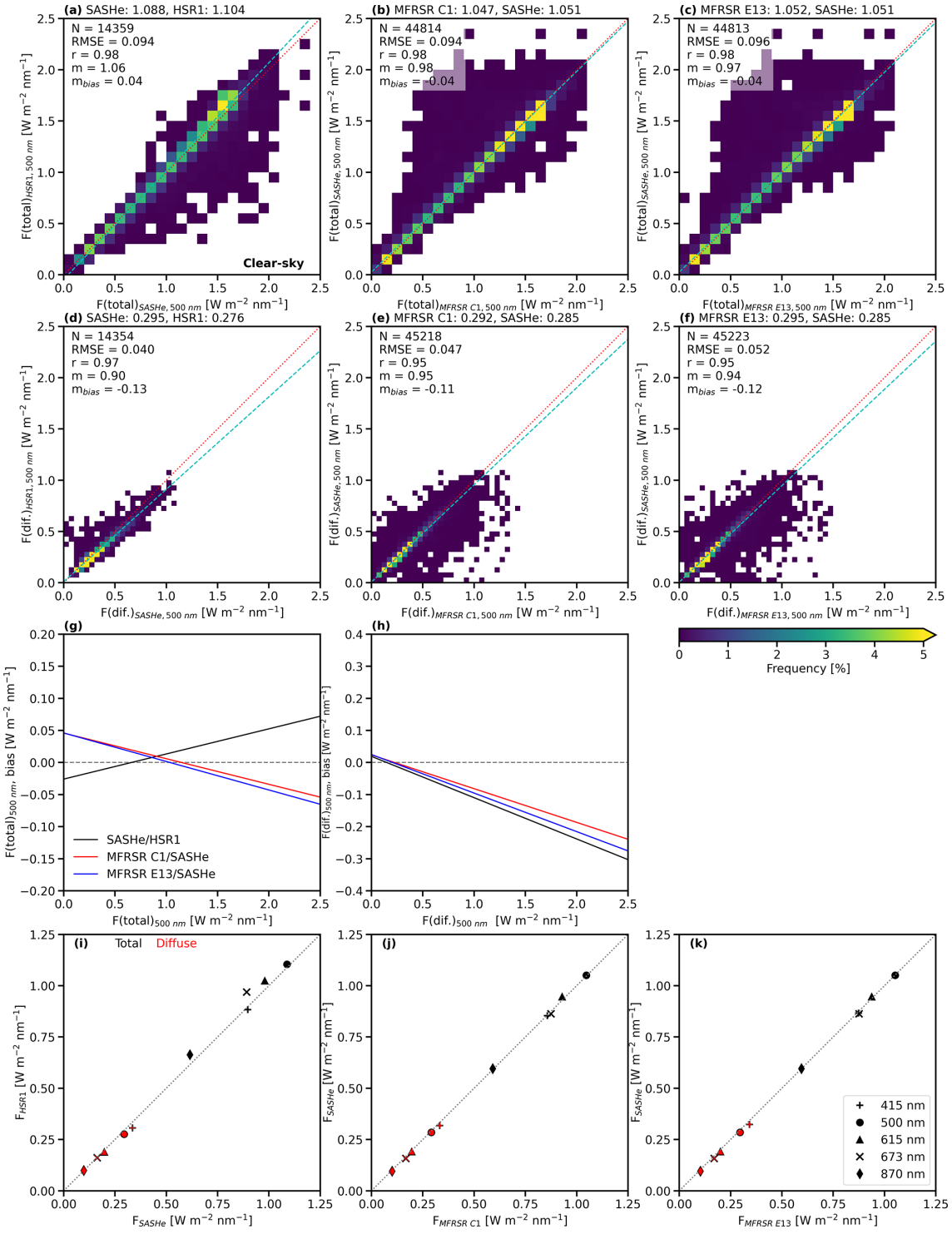

Figure 8. Frequency histogram for the clear-sky **(a–c)** F_{total} and **(d–f)** F_{diffuse} at 500 nm (W m^{-2} nm^{-1}) of the collocated **(a, d)** SASHe and HSR1, **(b, e)** MFRSR C1 and SASHe, and **(c, f)** MFRSR E13 and SASHe. The mean values are given above each plot. The N, RMSE, r, m, and m_{bias} are shown in the top left of each plot. The 1 : 1 line is indicated by the dotted red line, and the regression line is indicated by the dashed light-blue line. The regression lines of the **(g)** F_{total} and **(h)** F_{diffuse} bias are shown for SASHe and HSR1 (black), MFRSR C1 and SASHe (red), and MFRSR E13 and SASHe (blue). The zero line is indicated by the dashed gray line. **(i–k)** The mean clear-sky F_{total} (black) and F_{diffuse} (red) of collocated **(i)** SASHe and HSR1, **(j)** MFRSR C1 and SASHe, and **(k)** MFRSR E13 and SASHe at 415 nm (plus sign), 500 nm (circle), 615 nm (triangle), 673 nm (x mark), and 870 nm (diamond). The 1 : 1 line is indicated by the dotted gray line.

The mean differences in AOD are 0.01 or less, with less than 10 % relative differences (except for the MFRSR E13), which demonstrates excellent agreement. Furthermore, the mean difference between the CSPHOT AOD and the HSR1 AOD is within the CSPHOT's uncertainty of 0.01. For all the overlapping wavelengths, better AOD agreement is found for the other instruments compared to each other than with the HSR1, which is similar to the spectral irradiance comparison.

4.2.1 AOD at 500 nm comparison

The HSR1 AOD at 500 nm shows mean (relative) differences with the CSPHOT, MFRSR C1, MFRSR E13, and SASHe of 0.010 (8.0 %), 0.007 (6.4 %), 0.017 (17.7 %), and −0.008 (−6.2 %), respectively. With regression slopes less than 1 and negative slopes for the bias, this highlights that the HSR1 AOD is typically biased high at smaller AODs (∼ 0.05–0.10), except for the SASHe AOD, where the HSR1 AOD is biased low at larger AODs (∼ 0.30–0.40). In addition, the HSR1 AOD at 500 nm is within the uncertainty of the CSPHOT and MFRSR AODs (0.01; Table 1) of 28.1 %, 32.5 %, and 23.7 % of the time for the CSPHOT, MFRSR C1, and MFRSR E13, respectively.

In general, the HSR1 AOD is larger than those from the other instruments, except for those from the SASHe. Besides the MFRSR E13 AODs, the mean differences are 0.01 or less, with less than 10 % relative differences and high correlation coefficients, demonstrating excellent agreement in the AOD at 500 nm between the HSR1 AOD and the CSPHOT, MFRSR C1, and SASHe AODs. In particular, the mean difference of 0.010 between the CSPHOT AOD and the HSR1 AOD is encouraging, noting that the CSPHOT AOD uncertainty is 0.01 (Giles et al., 2019).

The CSPHOT, MFRSR C1, MFRSR E13, and SASHe AODs compare well with each other for AOD at 500 nm, with relative agreements between 2 % and 12 %. This comparison provides context to the HSR1 AOD comparison by quantifying the level of agreement between established instruments and AOD retrievals. For the CSPHOT AOD comparison, the mean (relative) differences with the MFRSR C1, MFRSR E13, and SASHe AODs are 0.007 (7.5 %), −0.004 (−4.4 %), and 0.014 (10.0 %), respectively. The mean (relative) differences in AODs between the MFRSR C1 and MFRSR E13, MFRSR C1 and SASHe, and MFRSR E13 and SASHe are −0.010 (−9.8 %), 0.002 (2.3 %), and 0.012 (12.0 %), respectively. The correlation coefficients are also large, with regression slopes near 1 and slightly negative regression slopes of the bias. The exception is the MFRSR AODs compared with the SASHe, where the regression slopes are larger than 1 instead of near 1 and the bias regression slopes are positive instead of negative. In addition, the MFRSR AODs at 500 nm are within the uncertainty of the CSPHOT AOD for 22.7 % and 78.2 % of the time for the MFRSR C1 and MFRSR E13, respectively. The SASHe AODs at 500 nm are within the uncertainty of the CSPHOT and MFRSR AOD for 33.5 %, 64.2 %, and 34.0 % of the time for the CSPHOT, MFRSR C1, and MFRSR E13, respectively.

Interestingly, the MFRSR AODs at 500 nm are within the uncertainty of each other only 18.2 % of the time, indicating more agreement with the CSPHOT than retrievals from the same instrument type. Similarly to the F_{total} and F_{diffuse} comparison, the MFRSR C1 and MFRSR E13 AOD comparison slightly disagrees, and that disagreement provides insight into part of the uncertainty of the measurement and AOD retrieval methods. The HSR1 AOD agrees with those from the other instruments, which is encouraging, indicating that some of the disagreement could be related to uncertainty inherent in the measurement and methods. The number of matching measurements for different instrument pairs are also quite variable, so the different comparisons may include different atmospheric conditions. This will also contribute to the variability between comparisons.

4.2.2 AOD at MFRSR wavelength comparison

The HSR1 mean clear-sky AODs were compared to mean AODs from the CSPHOT, MFRSRs, and SASHe for overlapping wavelengths (i.e., 415, 440, 500, 615, 673, 675, and 870 nm) in Fig. 10. The relative ordering in the AOD comparison at all the wavelengths is similar to those at 500 nm (Fig. 9): the mean HSR1 AOD is larger than those from the CSPHOT and the two MFRSRs, except for the mean SASHe AOD, which is larger than the mean HSR1 AOD.

The only spectral ranges where the HSR1 AOD is smaller than those from all the other instruments are at 415 nm (MFRSRs and SASHe) and 440 nm (CSPHOT). The mean spectral HSR1 AOD for the 415 and 440 nm channels is smaller than those from the CSPHOT, MFRSR C1, MFRSR E13, and SASHe by 8.2 %, 21.8 %, 14.4 %, and 23.1 %. For 440 and 500 nm, the mean spectral HSR1 AOD comparisons to the mean spectral CSPHOT AOD are within ∼ 8 % and ∼ 0.01.

In contrast, the disagreements in the 675 and 870 nm HSR1 and CSPHOT AOD comparisons are larger: 0.021 (25.8 %) and 0.030 (46.9 %), respectively. For the MFRSR AODs, better agreement is found between the HSR1 and MFRSR C1 AODs than between the HSR1 and MFRSR E13 AODs. The relative differences between the mean spectral HSR1 AOD and MFRSR C1 AOD are 25 % or less (except at 870 nm: 38.0 %). In contrast, the relative differences between the mean spectral HSR1 AOD and MFRSR E13 AOD are 14 %–18 % for the shorter wavelengths (i.e., 415 and 500 nm) but 35 %–66 % for the longer wavelengths (i.e., 615, 673, and 870 nm). In addition, the HSR1 AOD RMSE compared to the AODs of the CSPHOT and the MFRSRs increases with increasing wavelength for the 500–870 nm spectral range.

For the SASHe AOD, the HSR1 AOD is smaller by 10 % or less, except at 415 nm, where the HSR1 AOD is smaller by 23.1 %, and 870 nm, where the HSR1 is larger by 32.4 %.

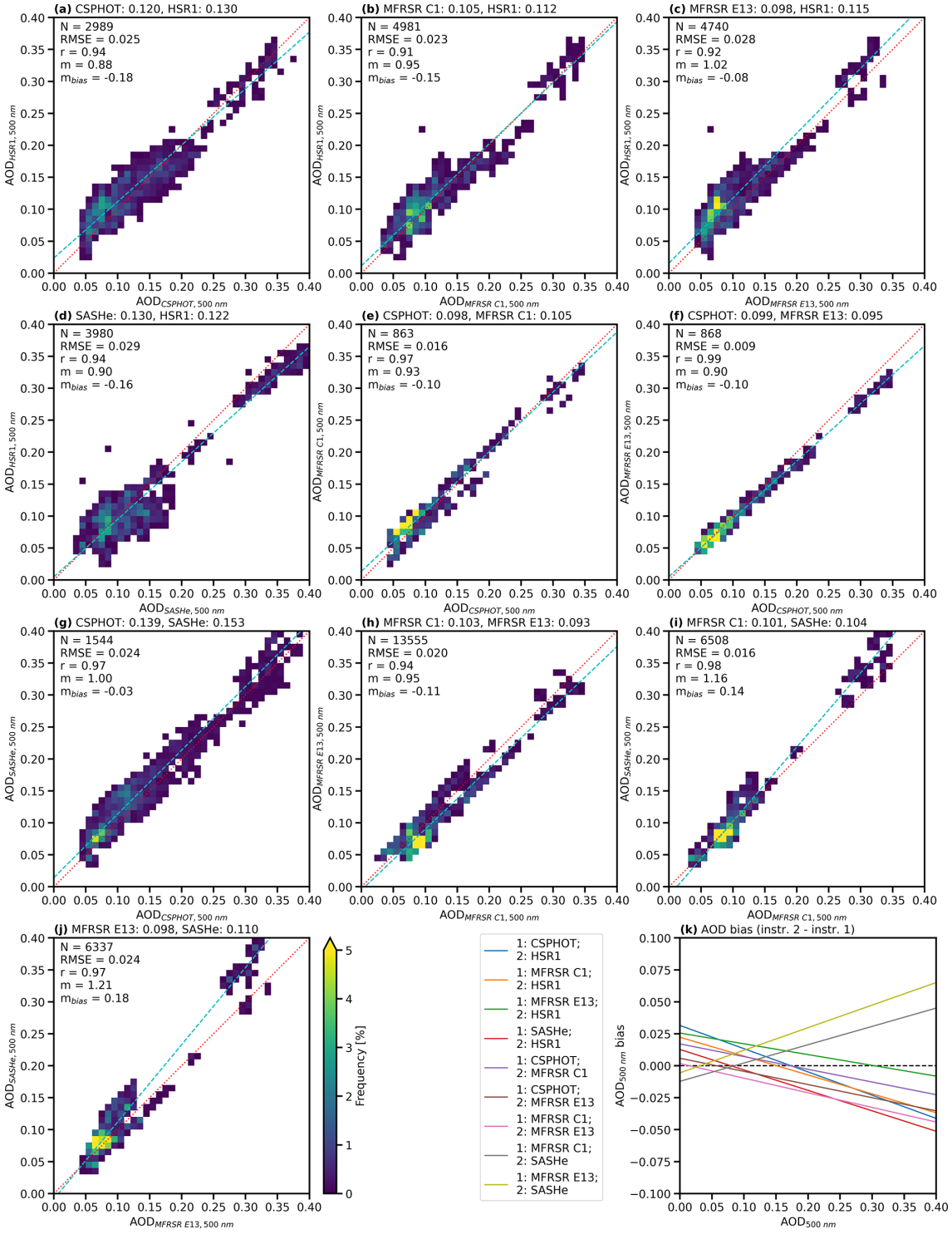

Figure 9. Frequency histogram for AOD at 500 nm of the collocated **(a)** CSPHOT and HSR1, **(b)** MFRSR C1 and HSR1, **(c)** MFRSR E13 and HSR1, **(d)** SASHe and HSR1, **(e)** CSPHOT and MFRSR C1, **(f)** CSPHOT and MFRSR E13, **(g)** CSPHOT and SASHe, **(h)** MFRSR C1 and MFRSR E13, **(i)** MFRSR C1 and SASHe, and **(j)** MFRSR E13 and SASHe. The mean values are given above each plot. The N, RMSE, r, m, and m_{bias} are shown in the top left of each plot. The 1 : 1 line is indicated by the dotted red line, and the regression line is indicated by the dashed light-blue line. **(k)** The regression lines of the bias are shown for each instrument comparison where the reference instrument (1) is compared to another instrument (2). The zero line is indicated by the dashed black line.

Except for 415 nm, the HSR1 AOD RMSE compared to the SASHe AOD is nearly the same value spectrally (~ 0.03).

The correlation coefficients are generally higher for smaller relative differences and are generally lower for larger relative differences in AOD. For example, the correlation coefficients are 0.91–0.95 for 415 and 500 nm but 0.61–0.86 for the 615, 673, and 870 nm HSR1 AOD comparisons. HSR1 AODs are less frequently within the uncertainty of the CSPHOT and MFRSR AODs for shorter and longer wavelengths compared to 500 nm. However, the value is consistent across the comparison, ranging from 15 % to 25 %, except for the HSR1 AODs within the MFRSR C1 at longer wavelengths (i.e., 615, 673, and 870 nm), where the value is 28 %–39 % of the time.

For context, the mean CSPHOT AOD was compared to the two MFRSR AODs and the SASHe AOD at the two overlapping wavelengths (i.e., 500 and 870 nm), and the mean AODs are largely found to agree well. The AOD comparison at 500 nm is described above. For 870 nm, the mean (relative) differences between the CSPHOT AOD and those from the MFRSR C1, MFRSR E13, and SASHe are 0.009 (18.3 %), -0.002 (-3.5 %), and 0.04 (6.0 %), respectively. The correlation coefficients are also large between the CSPHOT AOD and those from the other instruments (0.87–0.98). In addition, the AODs at 870 nm are within the uncertainty of the CSPHOT AOD for 25.0 %, 89.0 %, and 32.0 % of the time for the MFRSR C1, MFRSR E13, and SASHe, respectively. Interestingly, the MFRSR E13 AOD at 870 nm is again more often within the uncertainty of the CSPHOT AOD at 870 nm than the MFRSR C1 AOD at 870 nm (26.8 %).

The AODs from the two MFRSRs are compared to each other as well. The mean differences are all ~ 0.01, with relative differences of 8 %–17 %. The MFRSR AODs are within the uncertainty of each other for 30 % of the time at 415 nm, with lower relative frequencies at higher wavelengths of 615–870 nm (14 %–27 %). The MFRSRs and the SASHe AODs were also compared to each other. The SASHe AOD is typically larger than those from the two MFRSRs (2 %–41 %). The exception is when the SASHe AOD is smaller than the MFRSR AOD at 870 nm and for the MFRSR C1 AOD at 415 nm. The SASHe AODs are within the uncertainty of the MFRSR AODs for 21 %–49 % of the time. The AOD RMSE between the other instruments is the same as or smaller in value than the HSR1 AOD RMSE, which can be seen by comparing Fig. 10i to Fig. 10j. In general, better agreement is found between AODs derived from the other instruments than with the HSR1 AOD, particularly at longer wavelengths.

4.3 Diffuse ratio comparison

The HSR1 diffuse ratios were compared to the spectral diffuse ratios from the MFRSRs and SASHe in Fig. 11 and to the broadband diffuse ratios from RADFLUX in Fig. 12. This gives an irradiance comparison that is not dependent on the instrument calibration. It is also a useful quantity for looking at the impact of clouds on the irradiance.

For the spectral comparison, the mean (relative) diffuse ratio differences are typically ~ -0.05 or less (12 % or less) for the MFRSR wavelengths, except for the MFRSR diffuse ratio comparison at 940 nm, where the relative difference is ~ 19 %.

For the broadband comparison, the HSR1 mean integrated diffuse ratio is typically smaller than the broadband diffuse ratios by 0.04 (9 %). The similarity between the broadband and spectral diffuse ratio comparison suggests that the underestimation in the HSR1 F_{diffuse} measurements is the likely source of the broadband disagreement, more so than the HSR1 measuring a portion of the solar spectrum.

4.3.1 Spectral diffuse ratio comparison

As expected, the spectral diffuse ratio comparison reflects the fact that F_{total} has better agreement between instruments than F_{diffuse}. Overall, the HSR1 spectral diffuse ratio is typically smaller than those from the two MFRSRs at 500 nm, although general agreement is found with relative differences of 8 % (Fig. 11a, b). Similar to the F_{diffuse} comparison at 500 nm (Fig. 6), the mean HSR1 spectral diffuse ratio is smaller than those from the two MFRSRs at all other MFRSR wavelengths as well (not shown). For all the times, the mean HSR1 spectral diffuse ratio is smaller than those from both MFRSRs by 0.05 (10 %) or less at all the wavelengths except for 940 nm, where it is ~ 0.07 (~ 19 %). The results are similar when considering clear-sky times: HSR1 diffuse ratios are smaller than MFRSRs by 0.05 or less with relative differences of 12 % or less, except at 940 nm, where the relative difference is ~ 37 %.

The SASHe clear-sky spectral diffuse ratios were also compared at 415, 500, 615, 673, and 870 nm. The HSR1 diffuse ratio is smaller than the SASHe diffuse ratio by 6 % or less, except at 870 nm, where it is larger by 3 %. The SASHe diffuse ratio is smaller than those from the two MFRSRs by 2 % to 12 %. The diffuse ratios from the two MFRSRs were also compared to each other and indicate excellent agreement with relative differences of 0.8 % or less, except for 940 nm (4.2 %).

The high correlation (0.96–0.98) at 500 nm between the HSR1 and various instrument pairs is shown in Fig. 11a–c. This is similar to or slightly higher than the correlation between the MFRSRs and the SASHe (Fig. 11e, f) but does not match the near-perfect correlation between the two MFRSRs (Fig. 11d).

4.3.2 Broadband diffuse ratio comparison

The HSR1-integrated diffuse ratio is constructed by considering the F_{diffuse} and the F_{total}, both integrating from 400 to 1000 nm and then dividing the integrated F_{diffuse} by the integrated F_{total}. The HSR1-integrated diffuse ratios were

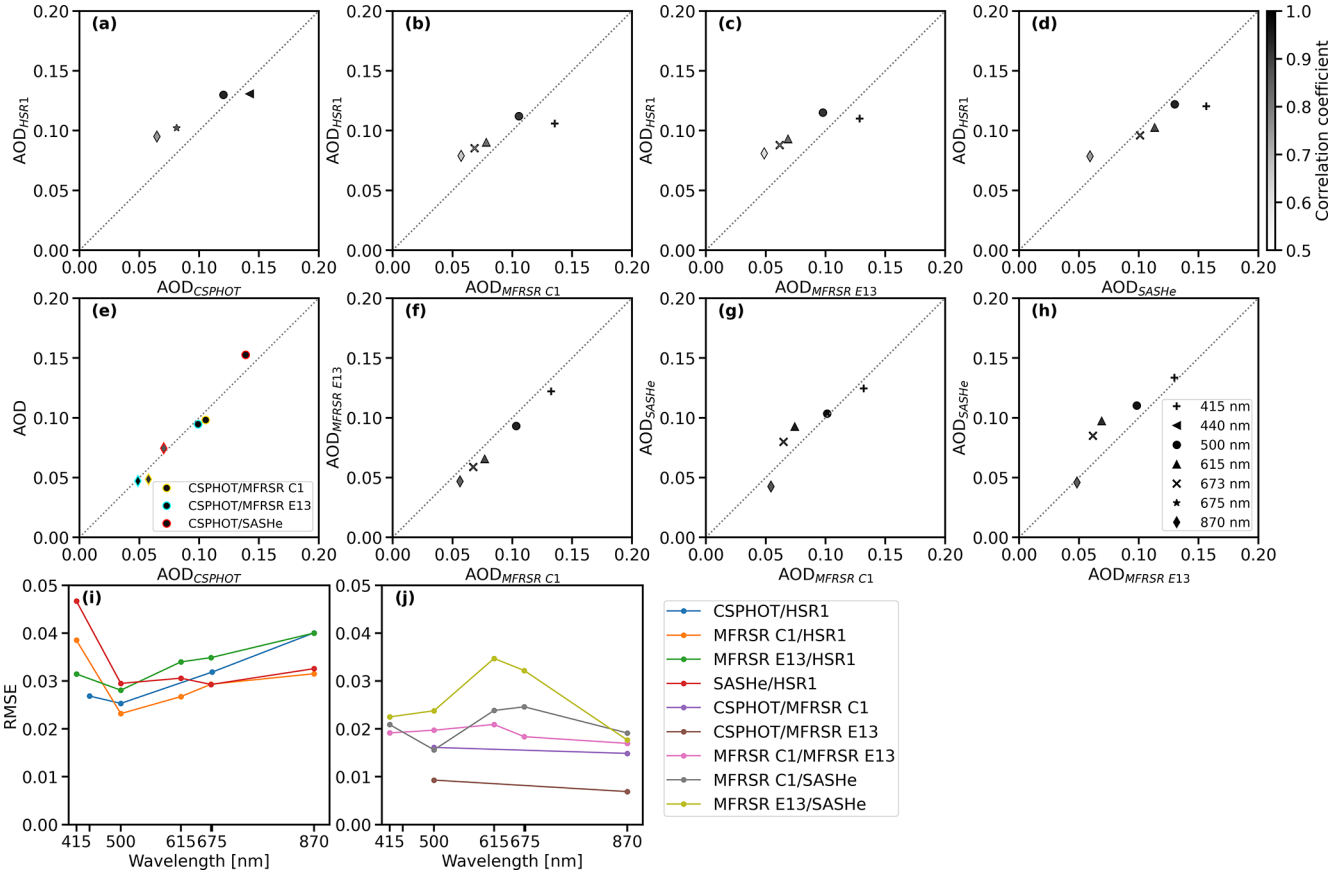

Figure 10. Mean AOD (black) of the collocated **(a)** CSPHOT and HSR1, **(b)** MFRSR C1 and HSR1, **(c)** MFRSR E13 and HSR1, **(d)** SASHe and HSR1, **(f)** MFRSR C1 and MFRSR E13, **(g)** MFRSR C1 and SASHe, and **(h)** MFRSR E13 and SASHe. The shading indicates the correlation coefficient. The mean AODs of the collocated CSPHOT with MFRSR C1 (yellow outline), MFRSR E13 (light-blue outline), and SASHe (red outline) are shown in panel **(e)**. The wavelengths considered include 415 nm (plus sign), 440 nm (left-pointing triangle), 500 nm (circle), 615 nm (triangle), 673 nm (x mark), 675 nm (star), and 870 nm (diamond). The 1 : 1 line is indicated by the dotted gray line. RMSEs are shown for **(i)** the HSR1 AOD and other instruments and **(j)** other instruments between each other.

compared to the broadband diffuse ratios from RADFLUX (Sect. 2.2.4). The motivation of this comparison is to understand whether the HSR1-integrated diffuse ratio captures the diffuse ratio in the absence of a diffuse solar broadband irradiance observation (e.g., only total broadband SW measurements) despite measuring only a portion of the solar spectral range.

The resultant diffuse ratio comparison is shown in Fig. 12. The HSR1-integrated diffuse ratio is found to typically be smaller than the broadband diffuse ratios. In terms of the mean diffuse ratio, the HSR1 diffuse ratio is smaller than the broadband diffuse ratio by 0.036 (8.5 %) for all the times (Fig. 12a) and 0.014 (7.8 %) for clear-sky times (Fig. 12b). The diffuse ratio comparison is also separated into overcast and partially cloudy skies (not shown), and the mean (relative) differences are 0.047 (−5.0 %) and 0.043 (−11.6 %), respectively. In general, the HSR1-integrated diffuse ratio is 12 % smaller or less, with closer agreement for clear skies under absolute difference and overcast conditions under relative difference and worse agreement during the dominant mode of partially cloudy skies, which accounts for ∼ 60 % of all the times.

To gauge the impact of the diffuse ratio error in terms of the irradiance errors, the error in the broadband diffuse irradiance ($F_{\text{broadband, diffuse}}$) is considered by comparing the broadband total irradiance ($F_{\text{broadband, total}}$) and HSR1-integrated diffuse ratio (DR_{HSR1}) to the $F_{\text{broadband,diffuse}}$:

$$F_{\text{diffuse, error}} = F_{\text{broadband, total}} \cdot \text{DR}_{\text{HSR1}} - F_{\text{broadband, diffuse}}. \quad (9)$$

The relative percent difference is shown in Fig. 12c, and the resultant irradiance error is shown in Fig. 12d. The mean $F_{\text{diffuse, error}}$ is −16.7 and −7.9 W m^{-2} for all times and clear-sky times, respectively. The measurement uncertainty of the $F_{\text{broadband,diffuse}}$ is ±3 % (Sect. 2.2.4). If the $F_{\text{broadband,diffuse}}$ is determined by the DR_{HSR1}, then the $F_{\text{diffuse, error}}$ values considering the DR_{HSR1} are within the $F_{\text{broadband, diffuse}}$ uncertainty only 16.5 % (all times) and 18.3 % (clear-sky times) of the time.

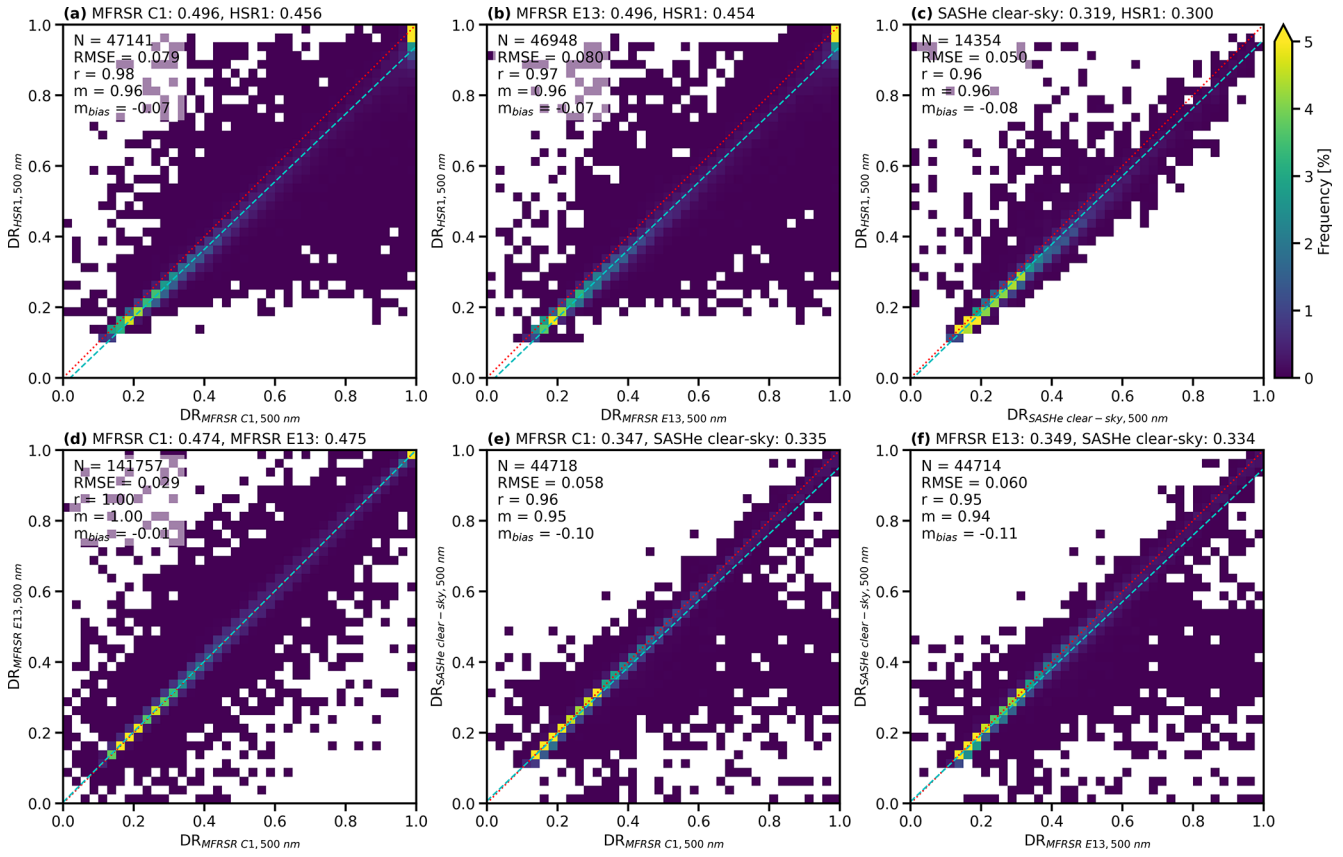

Figure 11. Frequency histogram for the diffuse ratio at 500 nm of the collocated **(a)** MFRSR C1 and HSR1, **(b)** MFRSR E13 and HSR1, **(c)** SASHe and HSR1, **(d)** MFRSR C1 and MFRSR E13, **(e)** MFRSR C1 and SASHe, and **(f)** MFRSR E13 and SASHe. The mean values are given above each plot. The N, RMSE, r, m, and m_{bias} are shown in the top left of each plot. The 1 : 1 line is indicated by the dotted red line, and the regression line is indicated by the dashed light-blue line. Note that SASHe diffuse ratios are limited to clear-sky conditions.

Interestingly, the broadband diffuse ratio comparison results are similar to those from the spectral diffuse ratio comparison (Fig. 11). This suggests that the low-biased HSR1 F_{diffuse} measurements due to the instrument design may be the dominant feature that explains the difference in the broadband diffuse ratio and not that the HSR1 measures less of the solar spectrum than a broadband radiometer. Furthermore, the smaller solar spectral range of the HSR1 would induce a high bias as the diffuse ratio decreases with increasing wavelength. This further suggests that the low bias in the HSR1 diffuse measurements is the dominant feature of the low diffuse ratio bias.

5 Discussion

In this study, the HSR1 is evaluated for future use as a hyperspectral radiometer. As shown in Figs. 5, 6, and 9, the HSR1 shows close agreement with both the MFRSR F_{total} and F_{diffuse} at 500 nm and with the CSPHOT AOD at 500 nm. This is encouraging and indicates that the HSR1 can give comparable results to these instruments at modest cost or in situations where the current instruments are difficult to operate, e.g., remote sites or moving platforms such as boats or planes. The ability of the HSR1 to give continuous measurements, in both time and spectrally, may also open up new opportunities.

5.1 Total irradiance measurements

As shown in the selected spectra in Fig. 2 and the summary comparisons in Figs. 7 and 10, the HSR1 spectral values are generally in good agreement at 415 and 500 nm, with the HSR1 measuring higher values at higher wavelengths. This pattern is in agreement with the extraterrestrial values calculated by the Langley process (see the later discussion).

The HSR1 continuous spectral measurements (as with the SASHe) can also be used to match specific spectral sensitivities, such as photosynthetically active radiation (PAR) for agricultural research, photopic eye response (illuminance) for architectural use, or photovoltaic (PV) panel sensitivities for PV research. An example comparison of the HSR1 with a Kipp & Zonen PAR sensor is shown in Appendix B.

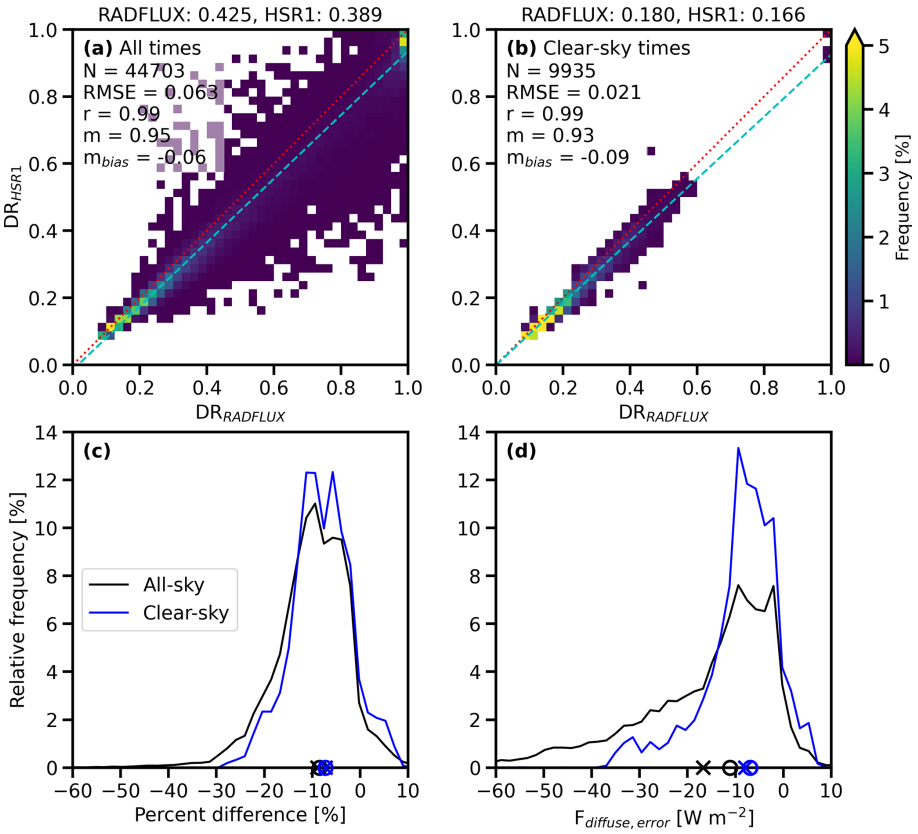

Figure 12. Frequency histogram for the collocated diffuse ratio (DR) between RADFLUX and HSR1 for **(a)** all times and **(b)** clear-sky times. The mean values are given above each plot, and the N, RMSE, r, m, and m_{bias} are shown in the top left of each plot. The 1 : 1 line is indicated by the dotted red line, and the regression line is indicated by the dashed light-blue line. Relative frequency plots of the **(c)** diffuse ratio percent difference between RADFLUX and HSR1 and **(d)** irradiance error in the broadband diffuse irradiance due to the HSR1-measured diffuse ratio ($F_{\text{diffuse, error}}$). The relative frequencies for all-sky times are in black, and for clear-sky times they are in blue. The mean value is denoted by an x mark, and the median is denoted by the open circle along the x axis.

5.2 Diffuse irradiance measurements

A distinctive feature of the comparisons in Fig. 4 is that the F_{diffuse} by the MFRSR is noticeably more variable under broken cloud conditions than the HSR1 measurement. This variation may be due to several possibilities.

1. The HSR1 measures both F_{total} and F_{diffuse} at the same time, whereas the MFRSR measures these sequentially during a 20 s scan of the shadowband.

2. The HSR1 measurements are averaged over a 1 min period with a 10 s sampling interval, whereas the MFRSR measurements are the 20 s closest to the HSR1 time. Fast-moving clouds can change the irradiance rapidly under these conditions.

3. It is possible that the various logger clocks are not always accurately aligned.

These differences in measurement and time synchronization would also explain the low-frequency background scatter of points in the irradiance comparison plots (Figs. 5 and 6).

The other distinctive feature is the low F_{diffuse} measurement of the HSR1 relative to all the reference instruments. This was also noted by Badosa et al. (2014) and is a feature of the shading-mask design. This low bias in F_{diffuse} has several possible causes.

1. The wide FOV of the HSR1 optics compared to the narrower FOV of the MFRSR, which means that forward-scattered circumsolar radiation is excluded from the HSR1 F_{diffuse} measurement but included in the MFRSR measurement, is able to measure the circumsolar component directly. Interestingly, the SASHe appears to show some similarities to the HSR1 in this regard. The circumsolar fraction increases with increasing AOD and cloud optical depth (COD) and hence F_{diffuse}. Both the SASHe and HSR1 show a reducing diffuse ratio with increasing diffuse irradiance, implying that more of the circumsolar irradiance is included in F_{direct} compared to the other references.

2. Manufacturing tolerances within the HSR1 shading mask may deviate from the assumption that the open areas are exactly 50 % of the full hemisphere.

5.3 AOD measurements

The HSR1 AOD calculation is based on the Langley method (Sect. 3), so it is independent of the HSR1 calibration accuracy and provides an independent check on the HSR1 calibration across those wavelengths where the Langley method applies.

At 500 nm, the two MFRSRs agree closely with each other and with the CSPHOT. The HSR1- and SASHe-derived AODs differ slightly more compared to each other and to the CSPHOT than comparisons between the filter-based instruments. The HSR1 RMSE compared to the CSPHOT is typically up to twice that of the MFRSRs and similar to the SASHe. This pattern is also shown in the RMSEs at other wavelengths (Fig. 10i, j).

The HSR1 AOD at 500 nm also shows a slope less than unity against the CSPHOT (Fig. 9a), as seen in previous comparisons (Wood et al., 2017). In the previous study, correlation with the CSPHOT was improved by an empirical correction. This has not been applied here, but further analysis will be presented in a future paper.

We also note that both the HSR1 and SASHe can generate spectrally continuous AOD measurements, though these are not shown here. These may enable us to distinguish between coarse and fine aerosols or cloud contamination, as suggested in Norgren et al. (2022).

5.4 Calibration

Calibration against a standard lamp provides a good starting calibration, but there may be improvements possible. The generally low light levels from the FEL lamp ($\sim 0.07\,\mathrm{W\,m^{-2}\,nm^{-1}}$) can be difficult to scale up to sunshine outdoors ($\sim 2\,\mathrm{W\,m^{-2}\,nm^{-1}}$) without introducing errors, which can affect the accuracy of measurement outdoors. They do, however, give a very smooth stable calibration over the whole spectral range.

The Langley method provides a comparison with the solar extraterrestrial (ET) spectrum in the wavelength ranges that are unaffected by gas absorption bands. As the HSR1 outputs are calibrated ($\mathrm{W\,m^{-2}\,nm^{-1}}$), the Langley intercept values should be the same as the known solar ET.

Figure 13 shows the solar ET spectrum from SMARTS2 v2.95 (Gueymard, 2004) smoothed to 3 nm bandwidth to match the HSR1 and the median of the Langley intercept values based on the HSR1 as originally calibrated. This shows a deviation similar to that shown in Fig. 2. Note also that this shows an HSR1 wavelength calibration offset of ~ 5 nm.

The Langley intercept corrected according to the post-deployment calibration check, and with the wavelength calibration offset applied, is also shown. This is in much better agreement with the solar ET – the RMSE between the Langley intercepts and the solar ET has halved from 0.16 to 0.08. This method may enable a continuing check on calibration during operation, as long as there are sufficient clear-sky periods to give a robust Langley calculation.

5.5 Future work

We have identified several areas for more detailed study, which we would hope to present in a later publication. These are described briefly here.

For AOD retrievals, the use of the full spectral range of the HSR1 may enable better AOD retrievals, in particular using the slope and spectral shape of the calculated optical depth from the HSR1 to determine the presence and quantity of light cloud in apparently clear skies (see Fig. 1 of Norgren et al., 2022, and the accompanying description). It may also be possible to improve the HSR1 AOD calculations by applying a correction for the wider FOV, as suggested in Wood et al. (2017), but with a better theoretical basis, as briefly described in Appendix A of Norgren et al. (2022). We would also like to explore the use of the HSR1 spectra for retrievals of other quantities such as water vapor or ozone.

In the area of instrument calibration, there are potential improvements to be made over the standard lamp calibration by using the Langley technique to correct or monitor the instrument calibration over time. The reasons for the low diffuse sensitivity should also be investigated and corrected where possible. The effects of correcting for the dome lensing variability first noted in Badosa et al. (2014) will also be investigated further and may reduce some of the variabilities in the F_{total}, F_{diffuse}, and retrieved AOD. Initial analysis indicates that the dome lensing effect on the results in this study are small, with a change of 0.01 or less in the F_{total}, F_{diffuse}, and AOD at 500 nm.

Other future instrument designs plan to address the measurement noise at the lower (below 400 nm) and upper (above 950 nm) wavelengths. The HSR1 demonstrated the capability to measure F_{total} and F_{diffuse} at wavelengths outside the spectral range focused on in this study of 400–950 nm (Fig. 2b, c). Future instrument designs plan to overcome the current prototype's noise, and the extended spectral range may be a high-quality measurable quantity in the future.

6 Conclusion

A new hyperspectral radiometer called the HSR1 was evaluated in terms of operability and performance in measuring surface irradiances and aerosol optical properties. This new instrument provides several distinct advantages and disadvantages compared to other instrumentation available for measuring spectral irradiances and AOD. The fixed-shading pattern that requires no moving parts makes this instrument unique among the instruments compared in this study. All

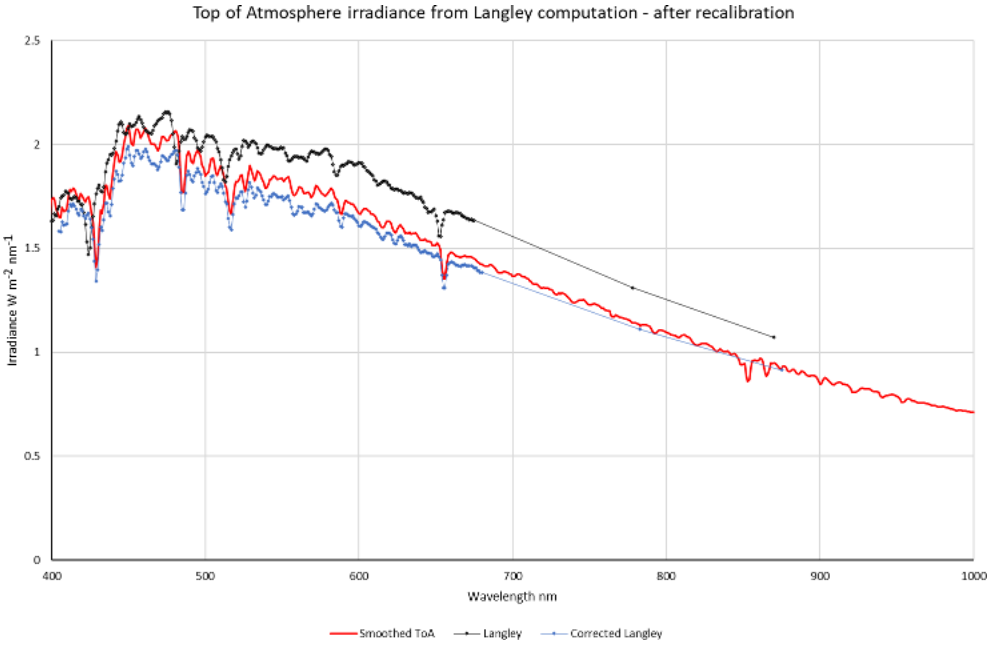

Figure 13. Extraterrestrial spectral irradiance from SMARTS2 (red), the Langley intercept values as calculated from the original HSR1 measurements (black), and the Langley intercept values adjusted according to the post-deployment calibration check with wavelengths adjusted to match the SMARTS2 spectral features (blue).

other instrumentation required alignment with the sun, which requires sun tracking and ultimately limits the ability of the instrumentation to operate in remote environments or on moving platforms (e.g., ships and aircraft). The trade-off, however, is that the wider FOV from this shading mask leads to inclusion of more of the circumsolar scattering in the direct rather than diffuse irradiance and a corresponding underestimation in diffuse irradiance that is wavelength-dependent. The evaluation analysis indicates that the mean AOD retrieved from the new hyperspectral radiometer is typically within uncertainty limits (0.01) of existing filter-based instruments, including a CSPHOT and two MFRSRs. There is, however, more wavelength-dependent systematic disagreement in AOD retrievals from spectrometer-based instruments and filter-based instruments than there is between different filter-based instruments. While spectrometers give unique and valuable information in the spectral dimension of the measurement, the lower signal-to-noise ratio in the measurements along with increased challenges from straylight detection at shorter and longer wavelengths lead to higher uncertainty in retrieved AODs than in filter-based instruments.

The analysis was limited to just irradiance and AOD comparisons in this study due to the number of comparison data sources available, although retrievals of other atmospheric and land surface properties are possible with hyperspectral measurements. The scientific need for hyperspectral radiometers will continue to increase in importance in the future as weather, climate, and renewable energy forecasting advance to incorporate spectral characteristics of aerosols and clouds. With the advancement of hyperspectral radiometers to meet this need, increased knowledge and process understanding of the atmosphere are possible.

Appendix A: SASHe description

The SASHe instrument used in this comparison is one of several shortwave array spectrometers that were designed and built for ARM through funding associated with the American Recovery and Reinvestment Act (ARRA). The SGP SASHe was installed in March 2011 and has been on site ever since. The SASHe provides measurements of solar irradiance components over the continuous spectral range from ultraviolet (UV) to the SW near-infrared (NIR). It uses a rotating shadowband technique similar to the MFRSR (Sect. 2.2.2) to alternately expose and shade a hemispheric diffuser (shown in Fig. A1a) to direct sunlight, thereby permitting measurements of direct, diffuse, and total irradiance components over a period of about 30 s. Light transmitted through the hemispheric diffuser is routed through a shutter assembly and connected to a pair of commercial Avantes fiber-coupled spectrometers (Fig. A1b) via large-core fused silica fiber. The measurement sequence operated by a laptop PC (Fig. A1c) includes "dark spectra" collected while the shutter is closed, followed by spectra collected while the shutter is open and the shadowband is in one of the following positions: (1) below the horizon so the diffuser is exposed to the entire sky, (2) "next to the sun" so that the band obscures a portion of the sky near the sun and the shadow falls just adjacent to the

diffuser, (3) casting a shadow directly across the diffuser, or (4) positioned so that the shadow falls just to the other side of the diffuser.

The SASHe calibration includes multiple elements described in more detail in the SASHe Instrument Handbook (Flynn, 2016) summarized here for convenience.

1. Wavelength registration of the spectrometer pixels versus published lines of a Hg–Ar emission lamp
2. Wavelength resolution varies from ~ 2.6 to ~ 2.3 nm over the UV/visible (VIS) spectral range.
3. Internal straylight levels confirmed to meet vendor specification of < 0.1 % over most of the spectral range. Empirical corrections have been applied for the short wavelength region.
4. External straylight leaking through fiber optic jacketing is confirmed to be negligible.
5. Diffuser angular response, a.k.a. "cosine correction", has been measured by rotating the SASHe diffuser through the full range of incident angle $\pm 90°$ relative to a broadband light source. This correction is most significant for the direct beam measurement, which also incorporates an implicit correction for spectrometer signal nonlinearity (discussed below). Effects of the diffuse angular response on the diffuse hemispheric component are modeled based on the measured direct beam correction. Both corrections are applied in routine processing.
6. Spectrometer signal linearity. A small but non-negligible nonlinearity has been identified. Normal processing of the direct beam signal removes this but does not remove effects on the diffuse hemispheric component which may contribute to differences observed in this study.
7. Nominal spectral response has been determined by reference to a spectrally calibrated quartz-tungsten-halogen (QTH) lamp positioned much closer than at the reference distance due to signal strength. This wavelength response curve is used only for pixels at wavelengths that are not amenable to Langley calibration, as noted below.
8. Langley calibration is conducted individually for all pixel wavelengths deemed not to be affected by water vapor or strong molecular absorbers as indicated in the SASHe ARM data files. The y intercept of a Langley plot represents what the instrument would measure at the TOA. Dividing the measurement by this amount yields the unitless atmospheric transmittance for each wavelength. Multiplying the unitless transmittance by extraterrestrial or TOA irradiance yields calibrated irradiance components in the same radiometric units as the reference source.

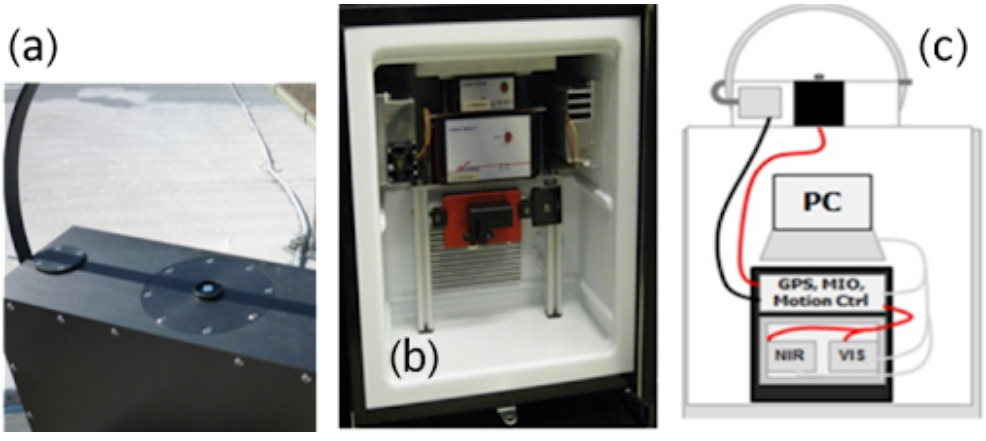

Figure A1. **(a)** SASHe optical collector with a shadowband casting a shadow over the hemispheric diffuser. **(b)** The SASHe chiller with spectrometers (top) and a shutter (red). **(c)** Schematic showing the collector on the outside of the building and umbilical connections to the PC, data acquisition, and spectrometers.

The SASHe data processing is conducted in a few distinct stages. First, the raw ASCII files generated by the instrument are converted into daily netcdf files. Second, the dark spectra and the irradiance components are identified by analysis of the raw spectra collected through the shadowband sequence, followed by cosine correction and application of a nominal irradiance calibration based on lamp measurements. Third, Langley regressions are applied to the log of the direct beam signal from each pixel versus the air mass. Depending on the conditions, a maximum of two Langley regressions is possible per day (one before noon and one afternoon), but typical atmospheric variations make these initial calibrations very noisy. Fourth, several weeks of the initial noisy data are filtered with an interquartile filter followed by a sliding Gaussian filter to obtain daily calibrations that vary by less than 1 % on average. Fifth, and finally, computation of the total optical depth (OD) comes from

$$\tau = \frac{\ln\left(\frac{I}{I_o}\right)}{m}, \tag{A1}$$

where τ is the total OD, I is the irradiance direct normal measurement, I_o is the smoothed Langley calibration at the TOA, and m is the optical air mass. AOD is computed from this by subtracting Rayleigh molecular OD at each wavelength and by subtracting ozone OD at affected wavelengths using the column abundance of ozone from the OMI (Sect. 2.2.6). ARM processing does not attempt other gas OD corrections, but suspect wavelengths are flagged with quality checks. Within the same processing stage, normalized transmittances are computed for each component I (i.e., direct normal, direct horizontal, diffuse hemispheric, and total hemisphere) divided by the TOA calibration I_o at the same wavelength. Lastly, each normalized transmittance component is multiplied by the extraterrestrial solar irradiance and adjusted for the earth–sun distance to yield the units (W m^{-2} nm^{-1}). Cloud-screened AODs are obtained using Alexandrov's normalized atmospheric variability method available in the data files and applied at quality-check flags.

As mentioned in Sect. 2.2.3, instrument issues affected operation of the SASHe during the HSR1 test period, which limited the SASHe comparison to clear-sky conditions. The instrument issues included a mechanical issue that led to frequent failure to clearly distinguish between the direct solar and diffuse hemispheric irradiance components, which was especially the case for cloudy skies. Additionally, a detector nonlinearity has been identified (but not yet corrected) that affects the diffuse irradiance values and thus also the total irradiance reported by the SASHe.

Appendix B: PAR comparison

PAR, integrated F_{total} from 400 to 700 nm, is measured by the PAR Quantum Sensor (PQS1) instrument as part of the Carbon Dioxide Flux Measurement System (CO2FLX) (Chan and Biraud, 2022). The measured PQS1 PAR is compared to the HSR1 PAR in Fig. B1. The mean (relative) difference for the HSR1 PAR compared to the PQS1 PAR is 53.9 (4.7 %) µmol m^{-2} s^{-1}. Better agreement is found for overcast conditions (−1.0 %) and worse agreement is found for clear-sky conditions (6.0 %). However, the spread in the PAR comparison is smallest for clear skies, noting that the correlation coefficient is highest (1.00) and the standard deviation of the difference is smallest (59.4 µmol m^{-2} s^{-1}). The spread in the PAR comparison is largely due to partially cloudy skies and overcast skies as the standard deviations of the differences are larger (∼ 130–210 µmol m^{-2} s^{-1}). The larger spread for the cloudy-sky PAR comparison may be partially due to clouds rapidly varying over time and space.

The HSR1 PAR is found by first converting the HSR1 F_{total} from W m^{-2} to µmol m^{-2} s^{-1} to match the PQS1 units by considering a spectral conversion factor (f) based on Planck's formula, such that

$$f = \frac{\lambda}{h\,c\,N_a} \times 10^{-3} = 0.00835935\lambda, \tag{B1}$$

where λ is the wavelength (nm), h is Planck's constant, c is the speed of light, and N_a is Avogadro's number. The spectral HSR1 values (µmol m^{-2} s^{-1}) are then integrated from 400 to 700 nm to obtain the HSR1 PAR.

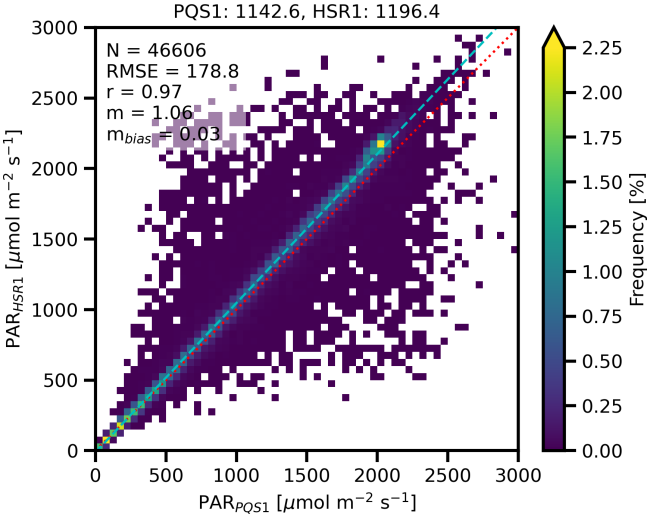

Figure B1. Frequency histogram for the collocated PAR (µmol m^{-2} s^{-1}) between the PQS1 and the HSR1. The mean values are given above the plot, and the N, RMSE, r, m, and m_{bias} are shown in the top left. The 1 : 1 line is indicated by the dotted red line, and the regression line is indicated by the dashed light-blue line.

For PQS1 PAR values below $\sim 1000\,\mu mol\,m^{-2}\,s^{-1}$, the collocated PAR observations with the highest frequency align along the 1 : 1 line with a mean difference of $45.7\,\mu mol\,m^{-2}\,s^{-1}$. Above $\sim 1000\,\mu mol\,m^{-2}\,s^{-1}$, HSR1 PAR values are biased high with a deviation from the 1 : 1 line and a mean difference of $67.6\,\mu mol\,m^{-2}\,s^{-1}$. However, the largest disagreement values switch from biased high to biased low near values of about $1500\,\mu mol\,m^{-2}\,s^{-1}$. This can be seen in the fact that the 1st (99th) percentiles of the differences are −219.8 (807.7) and −917.9 (326.1) $\mu mol\,m^{-2}\,s^{-1}$ for values below and above $1500\,\mu mol\,m^{-2}\,s^{-1}$, respectively.

The PAR comparison was separated into clear-sky, partially cloudy-sky, or overcast times (not shown). The mean (relative) differences are 86.2 (6.0 %), 64.3 (4.8 %), and −4.9 (−1.0 %) $\mu mol\,m^{-2}\,s^{-1}$ for clear-sky, partially cloudy-sky, and overcast times, respectively. This aligns with the results presented in Fig. B1, such that better agreement is found at lower values than at higher values, where higher values correspond more to clear-sky conditions and lower values correspond more to overcast conditions. While the mean difference is largest for clear skies, the spread in the comparison is smallest, noting that the correlation coefficient is the highest (1.00) and the standard deviation of the difference ($59.4\,\mu mol\,m^{-2}\,s^{-1}$) the smallest of the three conditions. This may suggest that, for clear skies, the conversion factor is too large or the HSR1 F_{total} is consistently too high in this spectral range. The spread in the PAR comparison in Fig. B1 is largely due to partially cloudy skies and overcast skies as the standard deviations of the differences are 210.3 and $129.6\,\mu mol\,m^{-2}\,s^{-1}$, respectively. The larger standard deviations may partially be a consequence of clouds rapidly varying over time and space.

While the PQS1 is utilized as a reference PAR measurement to evaluate the HSR1 PAR, there is no reported uncertainty for the PQS1 PAR and no traceable accurate reference for PAR measurements. Across different PAR instruments, the reported estimated PAR uncertainty is typically within 5 % for ideal conditions, but intercomparisons can be up to 20 % different, even for the same instrument (Mõttus et al., 2012). This suggests that the HSR1 PAR estimates are generally within measurement uncertainties of existing PAR instruments, even under different conditions.

Data availability. Data can be downloaded from the ARM data archive (https://www.arm.gov/data/, last access: 17 June 2024) for the HSR1 (sgphsr1C1.00; https://doi.org/10.5439/1888171; Atmospheric Radiation Measurement (ARM) user facility, 2022), CSPHOT (csphotaodfiltqav3; https://doi.org/10.5439/1461660; Gregory et al., 1994), MFRSRs (sgpmfrsr7nchaod1michC1.c1 and sgpmfrsr7nchaod1michE13.c1; https://doi.org/10.5439/1756632; Shippert and Shilling, 2021), ozone (gecomiX1.a1; https://doi.org/10.5439/1874262; Ermold, 2004), PAR (sgpco2flxrad4mC1.b1; https://doi.org/10.5439/1313017; Koontz et al., 2016), and RADFLUX (sgpradflux1longE13.c1; https://doi.org/10.5439/1395159, Riihimaki et al., 2020).

Author contributions. KAB, LDR, JW, CF, AT, and MR conceptualized the study. JW provided the HSR1 instrument and data. JW, AT, and MR provided project administration that facilitated the instrument deployment. CF, LM, GBH, and CH facilitated the operation and data processing of the comparison instruments. KAB and JW performed the formal analysis. KAB, JW, and CF prepared the figures. KAB drafted the manuscript. KAB, LDR, JW, CF, AT, LM, GBH, and CH reviewed and edited the manuscript.

Competing interests. John Wood is the inventor of the HSR1, and his company Peak Design Ltd. manufactures the HSR1. All the other authors declare that they have no conflict of interest.

Disclaimer. Publisher's note: Copernicus Publications remains neutral with regard to jurisdictional claims made in the text, published maps, institutional affiliations, or any other geographical representation in this paper. While Copernicus Publications makes every effort to include appropriate place names, the final responsibility lies with the authors.

Acknowledgements. Kelly A. Balmes and Laura D. Riihimaki thank Emiel Hall and Logan Soldo for their help in installing the HSR1 in Boulder. The authors also thank the SGP site technicians and all others who helped with the HSR1 test operations and corresponding logistics.

Financial support. This work was funded by the U.S. DOE ARM.

Review statement. This paper was edited by Sebastian Schmidt and reviewed by two anonymous referees.

References

Alexandrov, M. D., Lacis, A. A., Carlson, B. E., and Cairns, B.: Remote sensing of atmospheric aerosols and trace gases by means of multifilter rotating shadowband radiometer. Part I: Retrieval algorithm, J. Atmos. Sci., 59, 524–543, https://doi.org/10.1175/1520-0469(2002)059<0524:RSOAAA>2.0.CO;2, 2002a.

Alexandrov, M. D., Lacis, A. A., Carlson, B. E., and Cairns, B.: Remote sensing of atmospheric aerosols and trace gases by means of multifilter rotating shadowband radiometer. Part II: Climatological applications, J. Atmos. Sci., 59, 544–566, https://doi.org/10.1175/1520-0469(2002)059<0544:RSOAAA>2.0.CO;2, 2002b.

Andreas, A., Dooraghi, M., Habte, A., Kutchenreiter, M., Reda, I., and Sangupta, M.: Solar Infrared Radiation Station (SIRS), Sky Radiation (SKYRAD), Ground Radiation (GNDRAD), and Broadband Radiometer Station (BRS) Instrument Handbook, edited by: Stafford, R., ARM Climate Research Facility, DOE/SC-ARM-TR-025, https://doi.org/10.2172/1432706, 2018.

ARM user facility: Hyperspectral radiometer (HSR1), Atmospheric Radiation Measurement (ARM) user facility [data set], https://doi.org/10.5439/1888171, 2022.

Badosa, J., Wood, J., Blanc, P., Long, C. N., Vuilleumier, L., Demengel, D., and Haeffelin, M.: Solar irradiances measured using SPN1 radiometers: uncertainties and clues for development, Atmos. Meas. Tech., 7, 4267–4283, https://doi.org/10.5194/amt-7-4267-2014, 2014.

Chan, S. W. and Biraud, S. C.: Carbon Dioxide Flux Measurement System (CO2FLX) Instrument Handbook, edited by: Stafford, R., U.S. Department of Energy. DOE/SC-ARM/TR-048, https://doi.org/10.2172/1020279, 2022.

Ermold, B.: Ozone Monitoring Instrument (OMI), Atmospheric Radiation Measurement (ARM) user facility [data set], https://doi.org/10.5439/1874262, 2004.

Ermold, B., Flynn, C. J., and Barnard, J.: Aerosol Optical Depth Value-Added Product for the SAS-He Instrument, Version 1.0. U.S. DOE, Office of Science, Office of Biological and Environmental Research, DOE/SC-ARM/TR-133, https://doi.org/10.2172/1226568, 2013.

Flynn, C. J.: Shortwave Array Spectroradiometer–Hemispheric (SASHe) Instrument Handbook, edited by: Stafford, R., DOE ARM Climate Research Facility, DOE/SC-ARM-TR-172, https://doi.org/10.2172/1251414, 2016.

García-Cabrera, R. D., Cuevas-Agulló, E., Barreto, Á., Cachorro, V. E., Pó, M., Ramos, R., and Hoogendijk, K.: Aerosol retrievals from the EKO MS-711 spectral direct irradiance measurements and corrections of the circumsolar radiation, Atmos. Meas. Tech., 13, 2601–2621, https://doi.org/10.5194/amt-13-2601-2020, 2020.

Giles, D. M., Sinyuk, A., Sorokin, M. G., Schafer, J. S., Smirnov, A., Slutsker, I., Eck, T. F., Holben, B. N., Lewis, J. R., Campbell, J. R., Welton, E. J., Korkin, S. V., and Lyapustin, A. I.: Advancements in the Aerosol Robotic Network (AERONET) Version 3 database – automated near-real-time quality control algorithm with improved cloud screening for Sun photometer aerosol optical depth (AOD) measurements, Atmos. Meas. Tech., 12, 169–209, https://doi.org/10.5194/amt-12-169-2019, 2019.

Gregory, L., Sivaraman, C., Ma, L., and Wagener, R.: Sunphotometer (CSPHOTAODFILTQAV3), Atmospheric Radiation Measurement (ARM) user facility [data set], https://doi.org/10.5439/1461660, 1994.

Gueymard, C. A.: The sun's total and spectral irradiance for solar energy applications and solar radiation models, Sol. Energy, 76, 423–453, https://doi.org/10.1016/J.SOLENER.2003.08.039, 2004.

Hansen, J. E. and Travis, L. D.: Light scattering in planetary atmospheres, Space Sci. Rev., 16, 527–610, https://doi.org/10.1007/BF00168069, 1974.

Harrison, L. and Michalsky, J.: Objective algorithms for the retrieval of optical depths from ground-based measurements, Appl. Optics, 33, 5126–5132, https://doi.org/10.1364/AO.33.005126, 1994.

Harrison, L., Michalsky, J., and Berndt, J.: Automated multifilter rotating shadow-band radiometer: an instrument for optical depth and radiation measurements, Appl. Optics, 33, 5118–5125, https://doi.org/10.1364/AO.33.005118, 1994.

Harrison, L., Beauharnois, M., Berndt, J., Kiedron, P., Michalsky, J., and Min, Q.: The rotating shadowband spectroradiometer (RSS) at SGP, Geophys. Res. Lett., 26, 1715–1718, https://doi.org/10.1029/1999GL900328, 1999.

Hodges, G. B. and Michalsky, J. J.: Multifilter Rotating Shadowband Radiometer (MFRSR), Multifilter Radiometer (MFR), and Normal Incidence Multifilter Radiometer (NIMFR) Instrument Handbook, edited by: Stafford, R., DOE ARM Climate Research Facility, DOE/SC-ARM-TR-144, https://doi.org/10.2172/1251387, 2016.

Holben, B. N., Eck, T. F., Slutsker, I., Tanré, D., Buis, J. P., Setzer, A., Vermote, E., Reagan, J. A., Kaufman, Y. J., Nakajima, T., Lavenu, F., Jankowiak, I., and Smirnov, A.: AERONET – A Federated Instrument Network and Data Archive for Aerosol Characterization, Remote Sens. Environ., 66, 1–16, https://doi.org/10.1016/S0034-4257(98)00031-5, 1998.

Kasten, F. and Young, A. T.: Revised optical air mass tables and approximation formula, Appl. Optics, 28, 4735–4738, https://doi.org/10.1364/AO.28.004735, 1989.

Koontz, A., Hodges, G., Barnard, J., Flynn, C., and Michalsky, J.: Aerosol Optical Depth Value-Added Product Report, U.S. Department of Energy, DOE/SC-ARM/TR-129, https://doi.org/10.2172/1092419, 2013.

Koontz, A., Biraud, S., and Chan, S.: Carbon Dioxide Flux Measurement Systems (CO2FLXRAD4M), Atmospheric Radiation Measurement (ARM) user facility [data set], https://doi.org/10.5439/1313017, 2016.

Levelt, P. F., Joiner, J., Tamminen, J., Veefkind, J. P., Bhartia, P. K., Stein Zweers, D. C., Duncan, B. N., Streets, D. G., Eskes, H., van der A, R., McLinden, C., Fioletov, V., Carn, S., de Laat, J., DeLand, M., Marchenko, S., McPeters, R., Ziemke, J., Fu, D., Liu, X., Pickering, K., Apituley, A., González Abad, G., Arola, A., Boersma, F., Chan Miller, C., Chance, K., de Graaf, M., Hakkarainen, J., Hassinen, S., Ialongo, I., Kleipool, Q., Krotkov, N., Li, C., Lamsal, L., Newman, P., Nowlan, C., Suleiman, R., Tilstra, L. G., Torres, O., Wang, H., and Wargan, K.: The Ozone Monitoring Instrument: overview of 14 years in space, Atmos. Chem. Phys., 18, 5699–5745, https://doi.org/10.5194/acp-18-5699-2018, 2018.

Long, C. N. and Ackerman, T. P.: Identification of clear skies from broadband pyranometer measurements and calculation of downwelling shortwave cloud effects, J. Geophys. Res.-Atmos., 105, 15609–15626, https://doi.org/10.1029/2000JD900077, 2000.

Long, C. N., Ackerman, T. P., Gaustad, K. L., and Cole, J. N. S.: Estimation of fractional sky cover from broadband shortwave radiometer measurements, J. Geophys. Res.-Atmos., 111, 11204, https://doi.org/10.1029/2005JD006475, 2006.

McComiskey, A. and Ferrare, R. A.: Aerosol Physical and Optical Properties and Processes in the ARM Program, Meteor. Mon., 57, 21.1–21.17, https://doi.org/10.1175/AMSMONOGRAPHS-D-15-0028.1, 2016.

Michalsky, J. J. and Kiedron, P. W.: Moderate spectral resolution solar irradiance measurements, aerosol optical depth, and solar transmission, from 360 to 1070 nm, using the refurbished rotating shadow band spectroradiometer (RSS), Atmos. Meas. Tech., 15, 353–364, https://doi.org/10.5194/amt-15-353-2022, 2022.

Michalsky, J. J. and Long, C. N.: ARM Solar and Infrared Broadband and Filter Radiometry, Meteor. Mon., 57, 16.1–16.15, https://doi.org/10.1175/AMSMONOGRAPHS-D-15-0031.1, 2016.

Michalsky, J. J., Liljegren, J. C., and Harrison, L. C.: A comparison of Sun photometer derivations of total column water vapor and ozone to standard measures of same at the Southern Great Plains Atmospheric Radiation Measurement site, J. Geophys. Res.-Atmos., 100, 25995–26003, https://doi.org/10.1029/95JD02706, 1995.

Min, Q., Wang, T., Long, C. N., and Duan, M.: Estimating fractional sky cover from spectral measurements, J. Geophys. Res.-Atmos., 113, D20208, https://doi.org/10.1029/2008JD010278, 2008.

Mõttus, M., Sulev, M., Baret, F., Lopez-Lozano, R., and Reinart, A.: Photosynthetically Active Radiation: Measurement and Modeling, in: Encyclopedia of Sustainability Science and Technology, edited by: Meyers, R. A., Springer, New York, 7902–7932, https://doi.org/10.1007/978-1-4419-0851-3_451, 2012.

Norgren, M. S., Wood, J., Schmidt, K. S., van Diedenhoven, B., Stamnes, S. A., Ziemba, L. D., Crosbie, E. C., Shook, M. A., Kittelman, A. S., LeBlanc, S. E., Broccardo, S., Freitag, S., and Reid, J. S.: Above-aircraft cirrus cloud and aerosol optical depth from hyperspectral irradiances measured by a total-diffuse radiometer, Atmos. Meas. Tech., 15, 1373–1394, https://doi.org/10.5194/amt-15-1373-2022, 2022.

Riihimaki, L., Zhang, D., and Gaustad, K.: Radiative Flux Analysis (RADFLUX1LONG), Atmospheric Radiation Measurement (ARM) user facility [data set], https://doi.org/10.5439/1395159, 2020.

Riihimaki, L. D., Gaustad, K. L., and Long, C. N.: Radiative Flux Analysis (RADFLUXANAL) Value-Added Product: Retrieval of Clear-Sky Broadband Radiative Fluxes and Other Derived Values, edited by: Stafford, R., ARM user facility, DOE/SC-ARM-TR-228, https://doi.org/10.2172/1569477, 2019.

Riihimaki, L. D., Flynn, C., McComiskey, A., Lubin, D., Blanchard, Y., Chiu, J. C., Feingold, G., Feldman, D. R., Gristey, J. J., Herrera, C., Hodges, G., Kassianov, E., LeBlanc, S. E., Marshak, A., Michalsky, J. J., Pilewskie, P., Schmidt, S., Scott, R. C., Shea, Y., Thome, K., Wagener, R., and Wielicki, B.: The Shortwave Spectral Radiometer for Atmospheric Science: Capabilities and Applications from the ARM User Facility, B. Am. Meteorol. Soc., 102, E539–E554, https://doi.org/10.1175/BAMS-D-19-0227.1, 2021.

Shippert, T. and Shilling, J.: Aerosol Optical Depth (AOD) Derived from MFRSR Measurements (MFRSR7NCHAOD1MICH), Atmospheric Radiation Measurement (ARM) user facility [data set], https://doi.org/10.5439/1756632, 2021.

Turner, D. D., Mlawer, E. J., and Revercomb, H. E.: Water Vapor Observations in the ARM Program, Meteor. Mon., 57, 13.1–13.18, https://doi.org/10.1175/AMSMONOGRAPHS-D-15-0025.1, 2016.

Wang, T. and Min, Q.: Retrieving optical depths of optically thin and mixed-phase clouds from MFRSR measurements, J. Geophys. Res.-Atmos., 113, D19203, https://doi.org/10.1029/2008JD009958, 2008.

Wood, J. G.: Solar Radiation Sensor, European patent EP1012633 filed 4 September 1998, International patent WO 1999/013359, 18 March 1999.

Wood, J., Smyth, T. J., and Estellés, V.: Autonomous marine hyperspectral radiometers for determining solar irradiances and aerosol optical properties, Atmos. Meas. Tech., 10, 1723–1737, https://doi.org/10.5194/AMT-10-1723-2017, 2017.